

GL-TR-89-0140

Studies of Techniques for
Measuring Spaceborne Gaseous Contaminants
and Particulates in the Near Field

AD-A228 927

G.E. Galica
S.A. Rappaport
W.P. Reidy
O. Shepherd

Visidyne, Inc.
10 Corporate Place
South Bedford Street
Burlington, MA 01803

18 May 1989

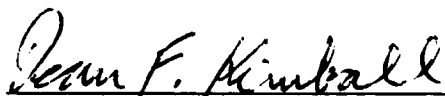
Scientific Report No. 2

Approved for Public Release; Distribution Unlimited

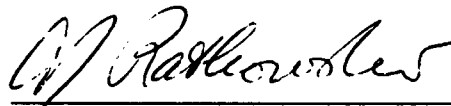
Geophysics Laboratory
Air Force Systems Command
United State Air Force
Hanscom Air Force Base, Massachusetts 01731-5000

DTIC
ELECTE
NOV 19 1990
S E D

"This technical report has been reviewed and is approved for publication"

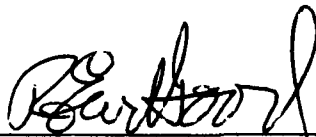


D. F. KIMBALL
Contract Manager
Atmospheric Backgrounds Branch
Optical and Infrared Technology Division



A. J. RATKOWSKI, Chief
Atmospheric Backgrounds Branch
Optical and Infrared Technology Division

FOR THE COMMANDER



R. EARL GOOD, SES, Director
Optical and Infrared Technology Division

This report has been reviewed by the ESD Public Affairs Office (PA) and is releasable to the National Technical Information Service (NTIS).

Qualified requestors may obtain additional copies from the Defense Technical Information Center. All others should apply to the National Technical Information Service.

If your address has changed, or if you wish to be removed from the mailing list, or if the addressee is no longer employed by your organization, please notify GL/IMA, Hanscom AFB, MA 01731. This will assist us in maintaining a current mailing list.

Do not return copies of this report unless contractual obligations or notices on a specific document requires that it be returned.

UNCLASSIFIED

SECURITY CLASSIFICATION OF THIS PAGE

REPORT DOCUMENTATION PAGE				Form Approved GMB No. 0704-0188	
1a REPORT SECURITY CLASSIFICATION UNCLASSIFIED			1b RESTRICTIVE MARKINGS		
2a SECURITY CLASSIFICATION AUTHORITY			3 DISTRIBUTION AVAILABILITY OF REPORT		
2b DECLASSIFICATION/DOWNGRADING SCHEDULE			Approved for Public Release; Distribution Unlimited		
4 PERFORMING ORGANIZATION REPORT NUMBER(S) VI-1284			5 MONITORING ORGANIZATION REPORT NUMBER(S) GL-TR-89-0140		
6a NAME OF PERFORMING ORGANIZATION Visidyne, Inc.		6b OFFICE SYMBOL (If applicable)		7a NAME OF MONITORING ORGANIZATION Geophysics Laboratory	
6c ADDRESS (City, State, and ZIP Code) 10 Corporate Place South Bedford Street Burlington, MA 01803			7b ADDRESS (City, State, and ZIP Code) Hanscom AFB, Massachusetts 01731		
8a NAME OF FUNDING SPONSORING ORGANIZATION		8b OFFICE SYMBOL (If applicable)		9 PROCUREMENT INSTRUMENT IDENTIFICATION NUMBER F19628-87-C-0072	
8c ADDRESS (City, State, and ZIP Code)			10 SOURCE OF FUNDING NUMBERS		
			PROGRAM ELEMENT NO	PROJECT NO	TASK NO
			62101F	3054	01
11 TITLE (Include Security Classification) Study of Techniques for Measuring Spaceborne Gaseous Contaminants and Particulates in the Near Field					
12 PERSONAL AUTHOR(S) G.E. Galica, S.A. Rappaport, W.P. Reidy, O. Shepherd					
13a TYPE OF REPORT Scientific #2		13b TIME COVERED FROM _____ TO _____		14 DATE OF REPORT (Year Month Day) 1989 May 18	
15 PAGE COUNT 64					
16 SUPPLEMENTARY NOTATION					
17 COSATI CODES			18 SUBJECT TERMS (Continue on reverse if necessary and identify by block number)		
FIELD	GROUP	SUB GROUP	spaceborne contaminants, water vapor contamination, particulate contamination, contamination modeling, flashlamps		
19 ABSTRACT (Continue on reverse if necessary and identify by block number)					
<p>Gaseous and particulate contamination pose a serious concern to the designers of spaceborne instrumentation. Water vapor is the most prevalent molecular species. Both molecular contaminants and particulates, when deposited on an optical surface, degrade the performance of sensitive optical instruments. Molecular and particulate contaminants in the field-of-view of an instrument also interfere with data collection and interpretation.</p> <p>This report outlines techniques for monitoring the water vapor and particulate contamination in the vicinity of a spacecraft. The water vapor concentration is measured by first dissociating the water vapor with VUV radiation from a krypton flashlamp and then monitoring the intensity of the chemiluminescence from the dissociation products. The particle properties are measured by illuminating particles in field of view of an imaging detector with visible radiation from a xenon flashlamp. The number of particles as well as the size and velocity distributions are obtained.</p>					
20 DISTRIBUTION/AVAILABILITY OF ABSTRACT <input type="checkbox"/> UNCLASSIFIED/UNLIMITED <input checked="" type="checkbox"/> SAME AS RPT <input type="checkbox"/> DTIC USERS			21 ABSTRACT SECURITY CLASSIFICATION UNCLASSIFIED		
22a NAME OF RESPONSIBLE INDIVIDUAL Dean Kimbal			22b TELEPHONE (Include Area Code) (617) 377-3642		22c OFFICE SYMBOL GL/OPB

UNCLASSIFIED

SECURITY CLASSIFICATION OF THIS PAGE

This report also describes models developed to predict the water vapor and particulate contamination environments in the vicinity of spacecraft. The models take into account previous spaceborne contamination measurements.

Accession For	
NTIS GRA&I	<input checked="checked" type="checkbox"/>
DTIC TAB	<input checked="checked" type="checkbox"/>
Unannounced	<input type="checkbox"/>
Justification	
By	
Distribution/	
Availability Codes	
Dist	Avail and/or Special
A-1	



TABLE OF CONTENTS

<u>Section</u>	<u>Page</u>
1 OVERVIEW	1
1.1 Motivation	1
1.2 Outline of Experiment Approach	1
2 DETECTION OF WATER VAPOR BY H ₂ O PHOTODISSOCIATION	2
2.1 Chemistry	2
2.2 Conceptual Experimental Design	8
2.3 Experiment Apparatus	8
2.3.1 Photolysis Radiation Source	8
2.3.2 Detectors	11
2.3.2.1 Krypton Radiometer	11
2.3.2.2 APL Imaging Spectrometer	11
2.3.3 Analysis of Detector Optics	11
2.3.4 Comparison of Axial and Perpendicular Geometries	16
2.4 Existing Measurements of Spaceborne H ₂ O Concentration	21
2.5 Calculations of Expected signal Levels	25
2.5.1 Derivation of Signal/Noise Expression for the Krypton Radiometer	25
2.5.2 Fractional Dissociation	30
2.6 Preliminary Flight Specifications	32
2.7 Topics Requiring Further Study	32
3 MEASUREMENT OF PARTICULATE CONCENTRATION	34
3.1 Particulate Scattering Phenomenology - Mie Scattering	34
3.2 Conceptual Design of the Experiments	34
3.3 Experimental Apparatus	34
3.3.1 Xenon Lamp	34
3.3.2 Detector	34
3.3.3 Detector Optics	37
3.4 Existing Measurements of Spaceborne Particulate Contamination	37
3.5 Calculation of Mie Scattering Cross-Sections	38
3.6 Calculations of Expected Signal Levels	44
3.6.1 Derivation of Signal/Noise Expression	44
3.6.2 Particle Velocity Effect on Signal Level	44
3.6.3 Estimation of Particle Detection Frequency	46

TABLE OF CONTENTS

<u>Section</u>	<u>Page</u>
3.7 Preliminary Flight Specifications	54
3.8 Topics Requiring Further Study	54
4 EXPERIMENTAL OPERATION	56
5 SUMMARY AND CONCLUSIONS	57
REFERENCES	58

LIST OF FIGURES

<u>Figure</u>		<u>Page</u>
1	Gaseous Contamination Measurement Chemistry	3
2	Fluorescence Spectrum of OH ($^2\Sigma^+$) After Photolysis of H ₂ O by 1236 Å Radiation. After Okabe ^[4]	4
3	H ₂ O Vapor Absorption Spectrum. After Herzberg ^[5]	5
4	Quantum Yield for OH (A → X) Emission as a Function of Photodissociation Wavelength. After Lee ^[2]	6
5	Rotational State Distribution for OH ($^2\Sigma^+$) for the Photo-dissociation of Water with 1236 Å Radiation. After Okabe ^[4]	7
6	Conceptual Drawing of the Water Vapor Detection Experiment	9
7a	Schematic Krypton Radiometers	12
7b	Preliminary Design for the Krypton Radiometer	13
8	Schematic Imaging Spectrometer	14
9	Axial and Perpendicular Geometries.	18
10a	Signal/Noise for the Krypton Radiometer, One Second Integration	28
10b	Signal/Noise for the Krypton Radiometer, 100 Second Integration	29
11	Fractional Dissociation of H ₂ O as a Function of Incident Flux	31
12	Conceptual Drawing of the Particulate Contamination Experiment	35
13	Spectral Irradiance from a 1000 W Xenon Flashlamp	36
14a	Differential Scattering Cross-Section for a 1 μm Ice Particle as a Function of Scattering Angle	42
14b	Differential Scattering Cross-Section for a 3 μm Ice Particle as a Function of Scattering Angle	43
15a	Detected Signal from a Single 3 μm Particle in a Single Pixel as a Function of Particle Velocity	48
15b	Detected Signal from a Single 1 μm Particle in a Single Pixel as a Function of Particle Velocity	49
16	Geometry Used for the Monte Carlo Particulate Outgassing Models	50

LIST OF TABLES

<u>Table</u>		<u>Page</u>
I	Proposed Krypton Lamps for the Water Vapor Detection Experiment	10
II	Sensitivities of the Krypton Radiometer and the APL Imaging Spectrometer in the Axial and Perpendicular Geometries	17
III	Out of Focus Sensitivities for the APL Imaging Spectrometer	22
IV	Previously Measured Spaceborne Water Vapor Concentrations	24
V	Preliminary Engineering Specifications for the Krypton Radiometer	33
VI	Previously Measured Spaceborne Particulate Detection Rates	39
VII	Differential Scattering Cross-Sections for the Various Size Ice Particles for 5000 Å Radiation and 90° Geometry	41
VIII	Examples Used for the Signal-to-Noise Calculation Shown in Figures 15a-b.	47
IX	Surface Fluxes and MSX Particle Detection Rates Derived from Previous Shuttle Measurements Through the Monte Carlo Modeling	51
X	Preliminary Engineering Specifications for the Xenon Unit	55

1. OVERVIEW

1.1 Motivation

A serious concern to designers of spaceborne experiments is the near field contamination from particulate matter and vapors released from the vehicle itself. As the spacecraft changes temperature, it expands and contracts releasing trapped water vapor and particulate matter. Dust particles, ice crystals, gaseous matter from thruster firings and cabin leaks as well as water adsorbed prior to launch contribute to the contamination problem. These materials contaminate sensitive optical surfaces and generate spurious signals. Molecular absorptions due to gaseous contaminants can also obscure and attenuate spectral data.

Water vapor, in particular, can lead to degradation of optical systems, particularly those used in the infrared, by depositing on cryogenically cooled optical surfaces. Particulates can manifest themselves in imaging systems by scattering sunlight or any other incident radiation. These signals can take the form of spurious resolved images as well as an increase in the background signal due to unresolved images.

Because of a lack of measured data, it is of scientific interest to characterize the near field concentration of water vapor and particulate matter in a spacecraft environment. It is also of interest to continuously monitor the contaminant levels on operational spacecraft in order to compensate for possible contamination effects.

1.2 Outline of Experimental Approach

Mie scattering provides the simplest experimental technique for characterizing particulate contamination. The near field is illuminated with visible radiation and the resulting scattered radiation is measured with the onboard APL UV/Visible Imager⁽¹⁾. The intensity yields information about the size and number of the particles. The tracking of the particles by the imaging detector provides information about the velocity of the particles.

Water vapor can be detected by various spectroscopic means. The technique chosen involves photodissociation of water vapor in the near field with VUV radiation and subsequent measurement of the emission from the electronically excited products. The intensity of the resulting radiation is directly related to the concentration of water vapor.

2. DETECTION OF WATER VAPOR BY H_2O PHOTODISSOCIATION

2.1 Chemistry

When a water molecule absorbs a photon in the 1350 - 1050 Å wavelength region, it dissociates with unit quantum yield into H atoms and either ground state or electronically excited state OH radicals (see Figure 1)^[2,3]. The excited state OH radicals then fluoresce efficiently in a rovibronic band at 3065 Å as shown in Figure 2^[4]. The Einstein A-coefficient for this fluorescence is $9 \times 10^5 \text{ sec}^{-1}$ ^[5].

Figure 3 shows the measured absorption spectrum for water in the 1200-1850 Å region^[5]. Figure 4 shows the quantum yield for production of the excited state OH radical as a function of photodissociation wavelength^[3]. Krypton lamps, having a strong emission line at 1236 Å, provide a convenient source for the photolysis radiation. The absorption coefficient, σ_{abs} , for water at 1236 Å is $2 \times 10^{-17} \text{ cm}^2 \text{ molecule}^{-1}$ and the quantum yield for production of the excited state OH radical, ϕ^* , is 0.07 for 1236 Å excitation. The effective photoemission cross-section, σ_{pe} , is then given by

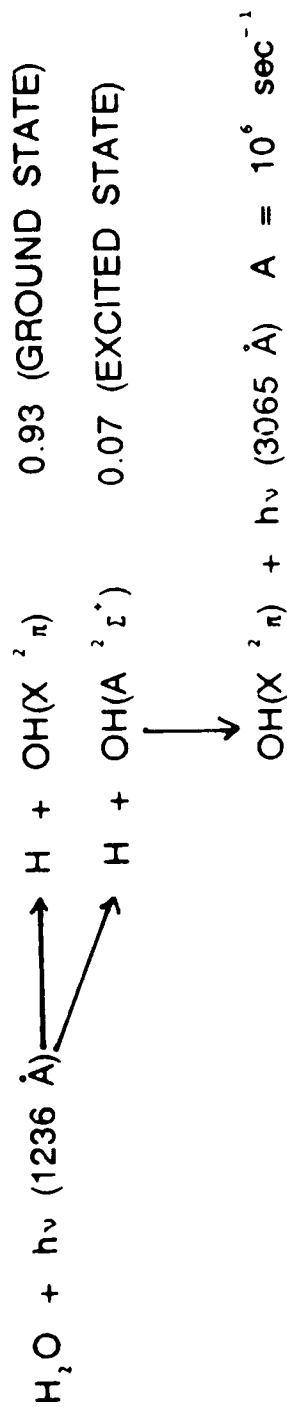
$$\sigma_{\text{pe}} = \sigma_{\text{abs}} \cdot \phi^*$$

and is equal to $1.4 \times 10^{-18} \text{ cm}^2 \text{ molecule}^{-1}$.

The ground and excited state OH radicals resulting from the photodissociation of H_2O are produced with a high degree of vibrational and rotational excitation^[4]. The vibrational distribution is roughly 1 : 0.3 : 0.1 for $v=0$: $v=1$: $v=2$. The rotational distribution is highly non Boltzmann and peaks at $N = 20$ (see Figure 5). Undissociated H_2O molecules also have thermal populations of excited vibrational and rotational states. The Infrared Radiometer band covers the 5-23 μm region; hence, molecules in some of these excited states, undergoing vibrational or rotational transitions, can be detected in the infrared^[1].

The $N=20 \rightarrow N=19$ rotational transition of OH ($v=0$) occurs at 13 μm and has a lifetime of 3.3 msec. Transitions from lower N rotational levels occur at longer wavelengths and consequently have longer lifetimes. Transitions from higher N rotational levels have shorter lifetimes, but these levels are not populated^[6]. The $v=1 \rightarrow v=0$ OH vibrational transition has a lifetime of 50 msec; however, this transition occurs at 2.8 μm - outside the bandpass of the

GASEOUS CONTAMINATION MEASUREMENT CHEMISTRY



$$\sigma_{\text{ABS}} = 2 \times 10^{-17} \text{ cm}^2$$

Figure 1. When a water molecule absorbs a photon in the 1050 - 1450 Å band it dissociates into an H atom and either ground or excited electronic state OH radicals. The excited state OH radicals fluoresce promptly in a band at 3065 - 3250 Å.

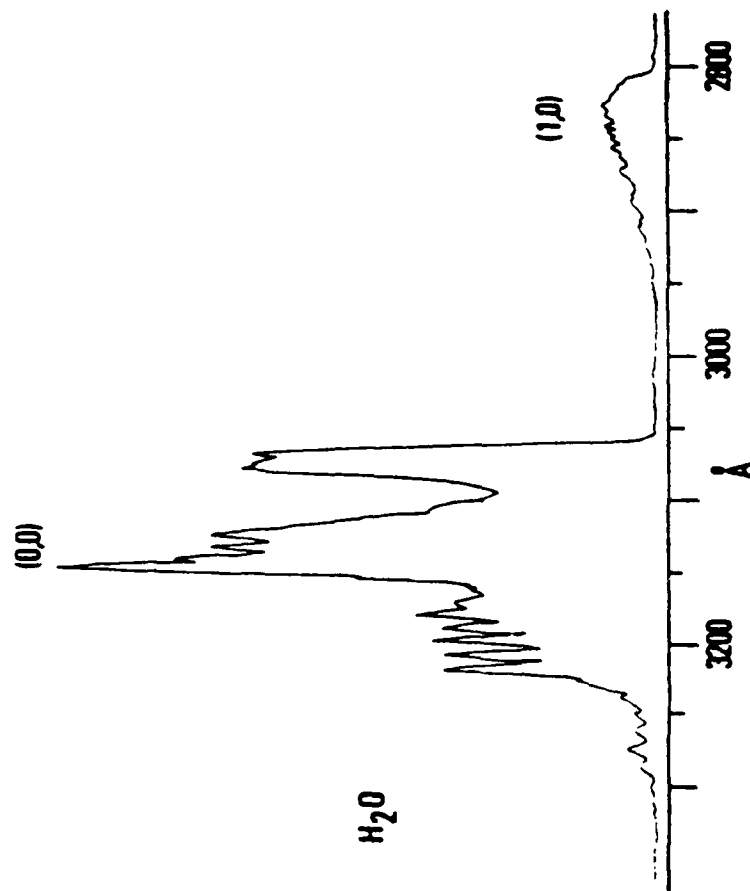


Figure 2. Fluorescence spectrum of QH_2 (Σ^+) after photolysis of H_2O by 1236 Å radiation. After Okabe.

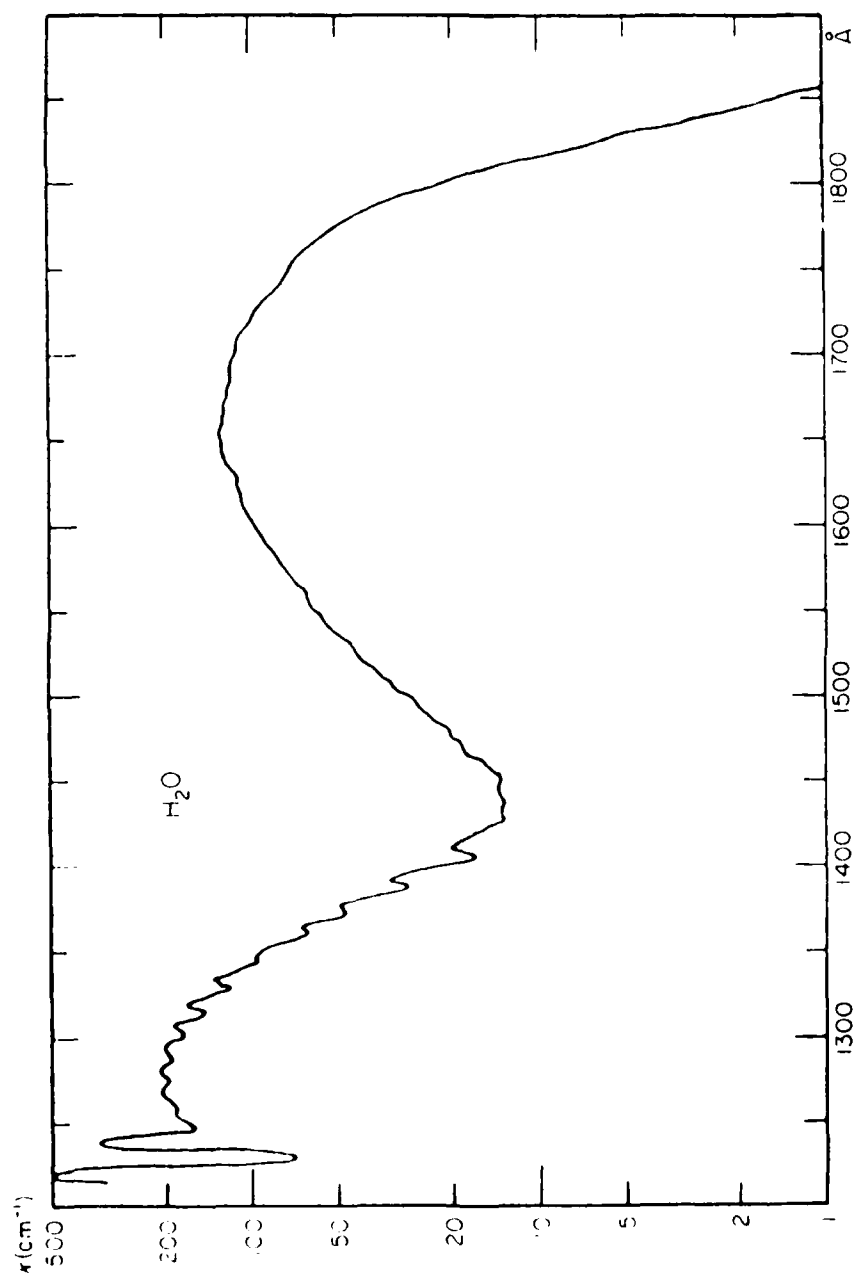


Figure 3. H₂O Vapor Absorption Spectrum, after Herzberg.³

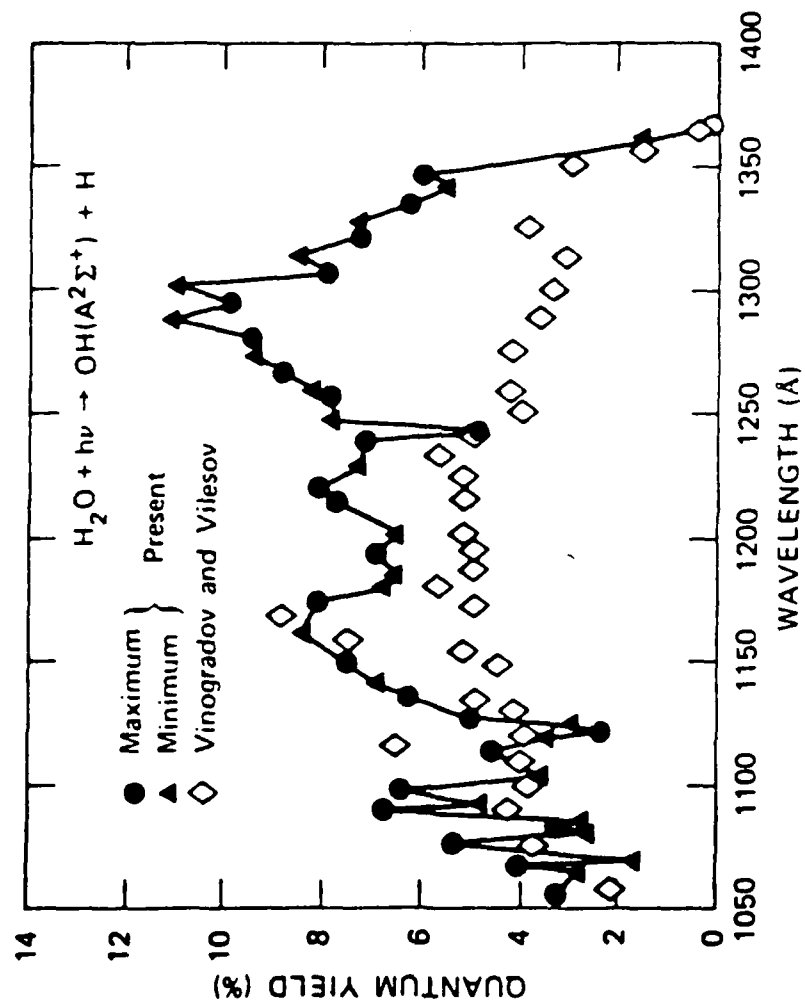


Figure 4. Quantum yield for OH ($\text{A} \rightarrow \text{X}$) emission as a function of Photodissociation Wavelength. After Lee.^{1a}

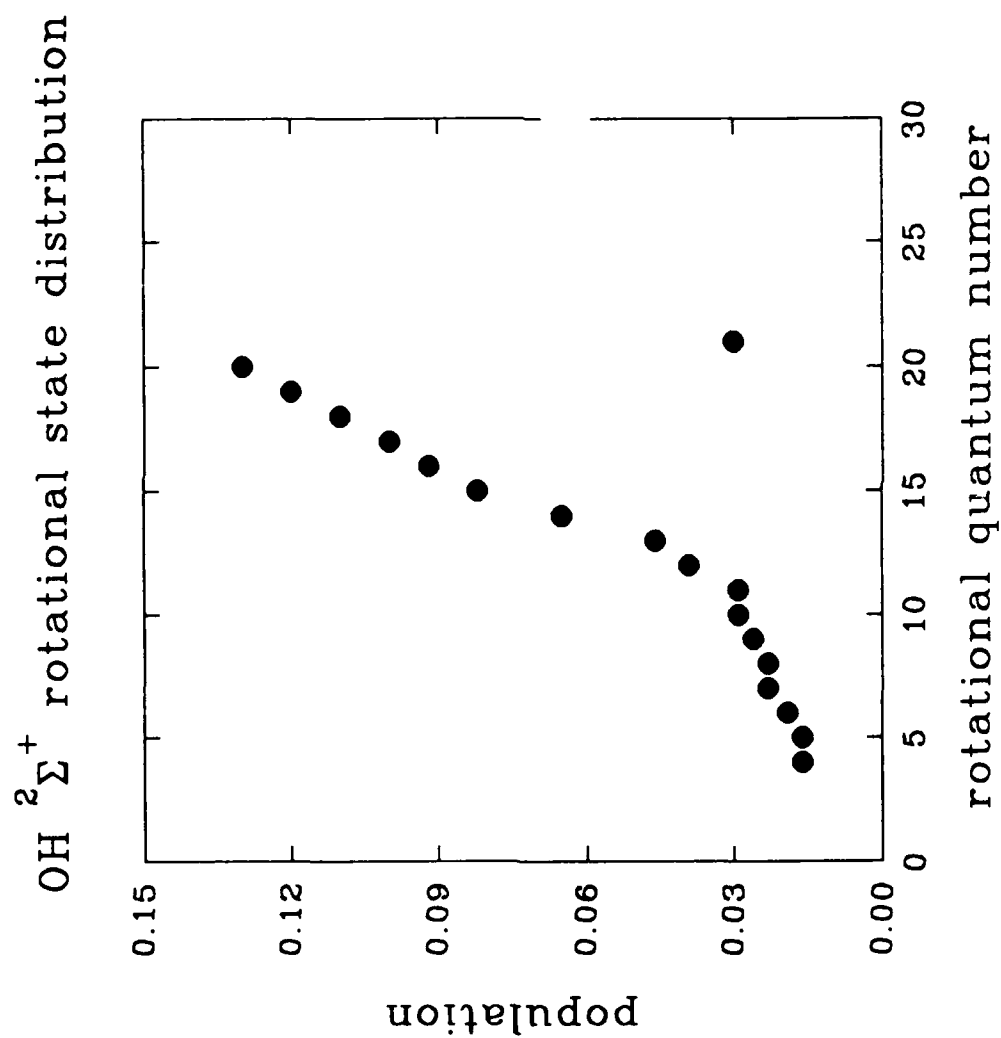


Figure 5. Rotational state distribution for $\text{OH } (^2\Sigma^+)$ for the photodissociation of water with 1236 Å radiation. After Okabe.^[4]

infrared radiometer. The H_2O molecule has several vibrational transitions within the infrared radiometer bandpass. The strongest ($14.98 \mu\text{m}$) has a lifetime of 360 msec. Given a thermal velocity of roughly $5 \times 10^4 \text{ cm sec}^{-1}$ and a viewing region with a characteristic dimension of six centimeters, most of the excited species will move out of the viewing region before emitting via these mechanisms limiting the usefulness of the Infrared Radiometer for detecting H_2O gaseous contamination.

2.2 Conceptual Experimental Design

A conceptual drawing of the experiment is shown in Figure 6. The output from a krypton lamp is collimated with an ellipsoidal reflector into a six cm diameter beam. The resulting OH ($A \rightarrow X$) fluorescence is detected either axially or at right angles to the incident beam. The active volume is assumed to fill the field of view of the detector.

2.3 Experimental Apparatus

2.3.1 Photolysis Radiation Source

Two continuous-wave krypton lamps are currently being considered as sources for the incident VUV radiation. The characteristics of each are given in Table I. Both lamps employ an RF-excited electrodeless discharge design and are manufactured by Resonance Ltd. The first lamp is a standard model, has low input power requirements and is already space qualified; however, the 1236 \AA output power of $5 \times 10^{14} \text{ photons sec}^{-1}$ is somewhat low for our needs. The second lamp is a custom modification of the previously described standard model. The modification includes an increase of the input power, use of a MgF_2 capillary and an increase of the capillary volume. The expected 1236 \AA power output is $8 \times 10^{15} \text{ photons sec}^{-1}$ - a sixteen-fold improvement over the standard model.

Advantageously, most of the radiation occurs as line emission with very little continuum radiation being produced by the RF-excited discharge lamp. Also no krypton emission lines are present in the main part of the OH ($A \rightarrow X$) emission band^[7]. Because no electrodes are employed in this lamp design, the lamp's spectral output contains few impurity features. Also, the cooling requirements of this lamp are minimal. The lamp will be operated with a 50% duty cycle and have pulse widths of 500 msec.

CONCEPTUAL PHOTODISSOCIATION GEOMETRY

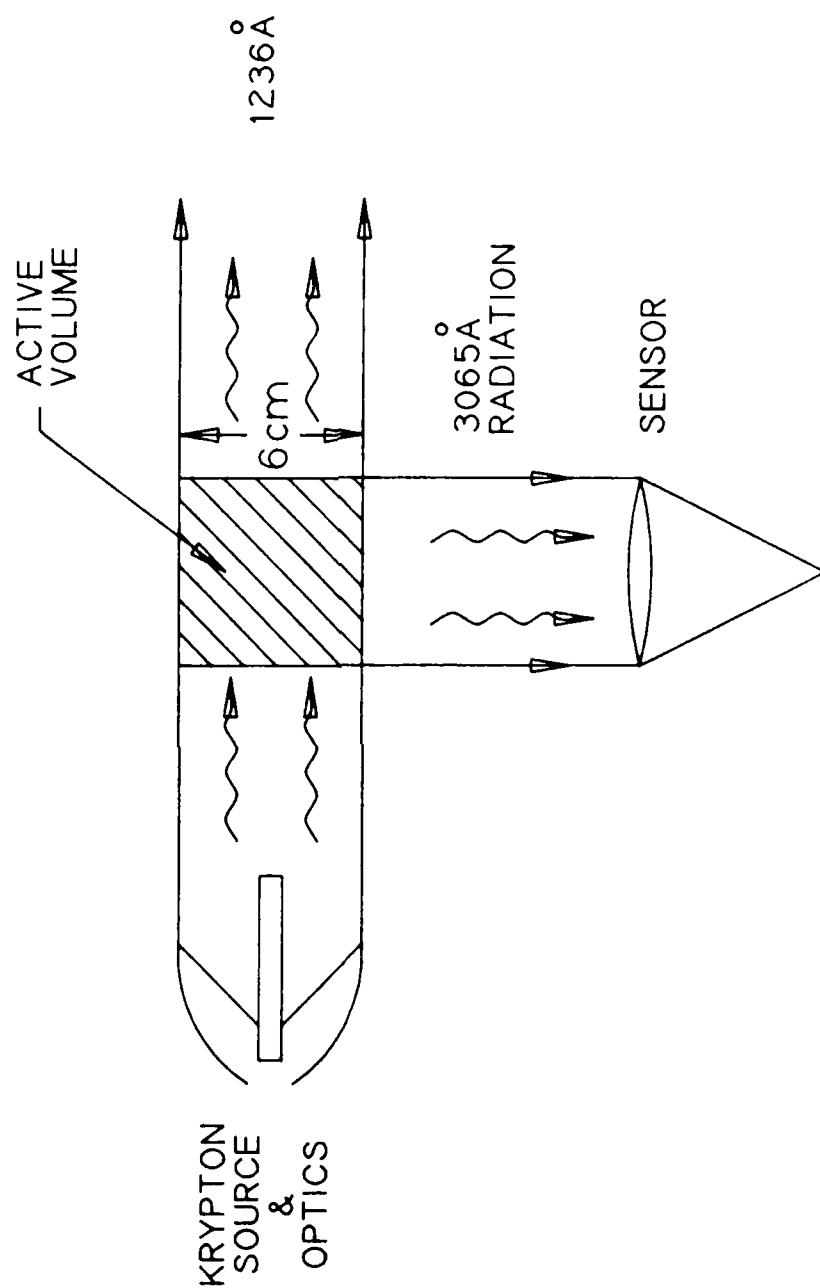


Figure 6. Conceptual drawing of the water vapor detection experiment. The experiment can be performed in either the perpendicular geometry (as shown) or in the axial geometry (detecting along the incident beam).

Table I

Proposed Krypton Lamps for the Water Vapor Detection Experiment

	<u>Type</u>	<u>MFG</u>	<u>Characteristics</u>	<u>Power In</u>	<u>Output Photons Sec</u>
1	RF Excited Electrodeless Discharge	Resonance Ltd.	Space Qualified	15 W	5×10^{14}
2	RF Excited Electrodeless Discharge	Resonance Ltd.	High Intensity, MgF ₂ Capillary Reflective Focusing Optics	100 W	8×10^{15}

Photon Flux (f)

Assume 50% of Photons Collimated in 6 cm Diameter Beam

Type 1; $f = 8.8 \times 10^{12}$ (Photons $\text{cm}^{-2} \text{S}^{-1}$)

Type 2; $f = 1.4 \times 10^{14}$ (Photons $\text{cm}^{-2} \text{S}^{-1}$)

2.3.2 Detectors

We are proposing that two types of detectors be used for the water vapor detection experiment. One detector, the Krypton Radiometer, will be built as part of the lamp package. The other will be one or more of the APL Imaging Spectrometers.

2.3.2.1 Krypton Radiometer

This detector will be a filtered EMR type 541 photomultiplier tube having a bialkali photocathode. This PMT has a one inch photocathode, a quantum efficiency of 0.1, and a dark current of 14 counts sec^{-1} at 293°K. The filter transmission is approximately 50%.

The collection optics will be an f/1 system having a focal length of 5 cm. The distance from the collection optics to the radiating volume is 10 cm. The area of the collecting optics is approximately 25 cm^2 . A schematic representation of the Krypton Radiometer is shown in Figure 7a and a preliminary design is shown in Figure 7b.

The Krypton Radiometer provides a small, integral unit for testing and calibration of the experiment. It is inexpensive and it provides a sensitive, efficient measure of the water vapor concentration.

2.3.2.2 APL Imaging Spectrometer

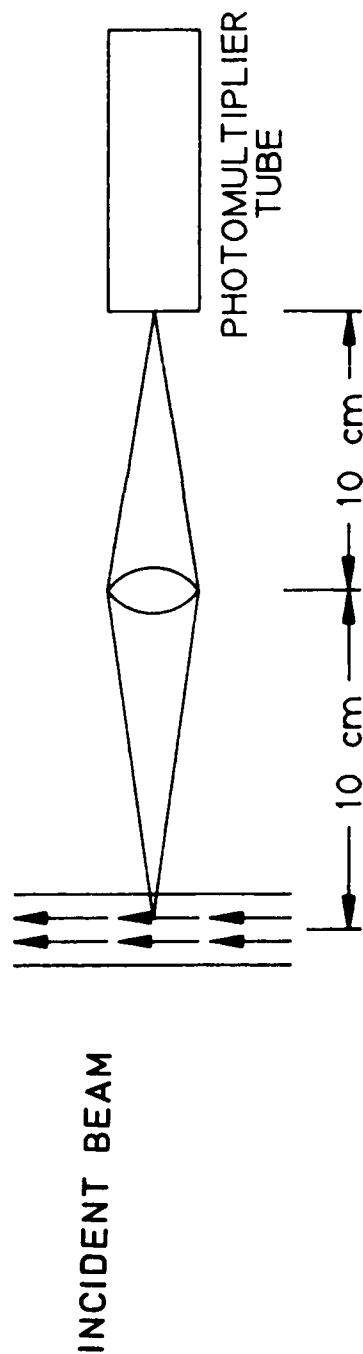
In addition to the Krypton Radiometer, it is desirable to obtain spectrally resolved data with the APL Imaging Spectrometer to provide more positive identification that the emission is that of OH and to determine if there are other species emitting in the region illuminated by the lamp⁽¹⁾. There are five APL Imaging Spectrometers covering various wavelength bands. The instantaneous angular resolution of each spectrometer is 0.1 x 1.0 degrees. The collection optics have an area of 100 cm^2 , a focal length of 48 cm and are focused at infinity. The Imaging Spectrometer is shown schematically in Figure 8.

2.3.3 Analysis of Detector Optics

Since no modification to the APL Imaging Spectrometer optics will be provided, a detailed analysis of the optics must be made. The APL imaging spectrometer is shown schematically in Figure 8. the collection optics have a focal length of 48 cm and are focused at infinity. The slit plane is located one focal length away from the collection optics so that objects at infinity will be focused on the slit. The slit dimensions are 0.84 x 0.084 cm.

Krypton Radiometer

90-354



COLLECTION OPTICS

$A = 25 \text{ CM}^2$
 $f = 5 \text{ CM}$
 1/1 MAGNIFICATION
 FOCUSED AT 10 CM

PMT

FILTERED EMR TYPE 541 PMT, BIALKALI PHOTOCATHODE
 14 DARK COUNTS SEC^{-1} AT 293°K
 QUANTUM EFFICIENCY $\eta = .1$

Figure 7a. Schematic of the Krypton Radiometer.

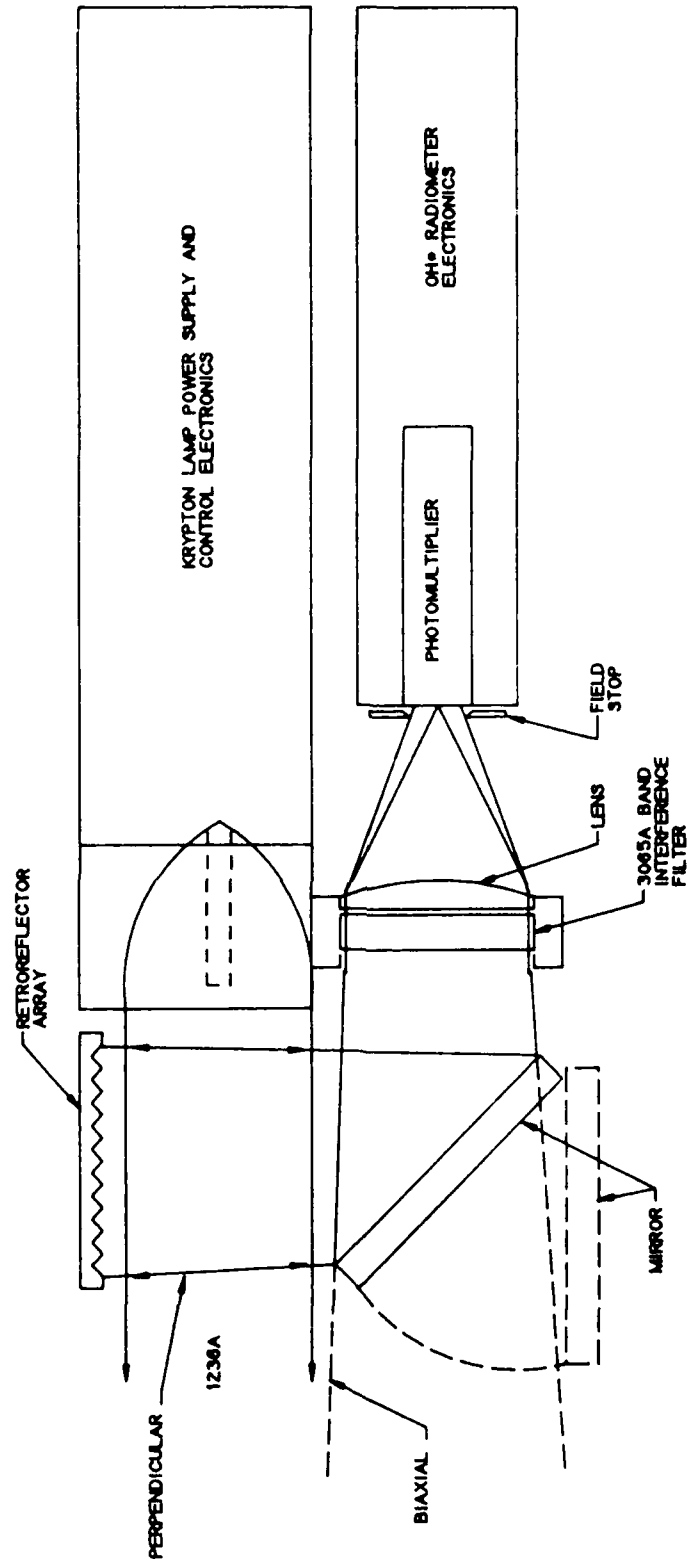
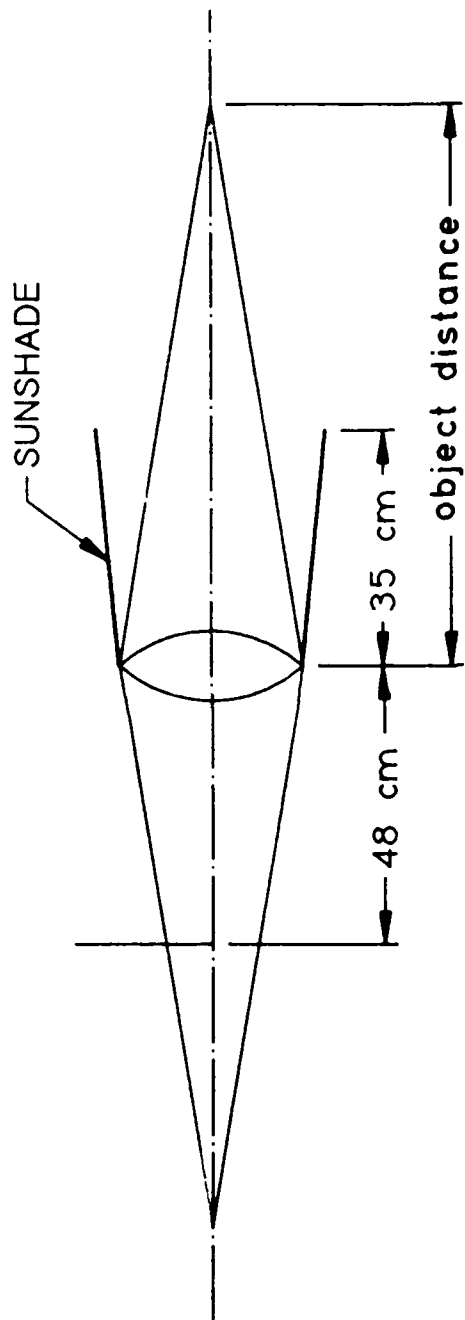


Figure 7b. Preliminary design for the Krypton Radiometer.

Schematic Imaging Spectrometer

90-355



$f = 48 \text{ CM}$ FOCUSED AT INFINITY

$A = 100 \text{ CM}^2$

INSTANTANEOUS FOV $1.0 \times 0.1^\circ$

SCAN FOV $1.0 \times 1.0^\circ$

SLIT SIZE $0.84 \times 0.084 \text{ CM} - 7 \times 10^{-2} \text{ CM}^2$

Figure 8. Schematic Imaging Spectrometer.

When in focus assuming the field of view is filled, the differential signal is given by

$$dS = \gamma \cdot \Omega \cdot dr$$

$$\gamma = \frac{1}{4\pi} \cdot f \cdot \sigma_{pe} \cdot [H_2O] \cdot \eta \cdot T \cdot R_d \cdot A_{tel}$$

where f is the incident flux expressed in photons $\text{cm}^{-2} \text{ s}^{-1}$, σ_{pe} is the photoemission cross-section expressed in $\text{cm}^2 \text{ molecule}^{-1}$, $[H_2O]$ is water vapor density in molecules cm^{-3} , η is the detector quantum efficiency, T is the filter transmission R_d is the duty cycle, A_{tel} is the area of the collection optics, Ω is the solid angle of the detector, and dr is the differential length along the line-of-sight. When out of focus, the differential signal is given by

$$dS = \gamma \cdot \int Q \frac{dA_o}{r^2} dr$$

where

$$\Omega_{eff} = \int Q \frac{dA_o}{r^2}$$

where dA_o is an element of area in the object plane, r is the distance to dA_o , Q is the fraction of light incident on the slit plane which actually passes through the slit. and the integral is over the object plane.

There are several factors which limit the value of the above integral. The physical size of the radiating region, external baffling on the optics, and limits on the acceptance angle for the radiation entering the slit will restrict the effective field of view.

As an example, we can compare the in-focus and out-of-focus signals for the Imaging Spectrometer when the 6 cm diameter incident beam is in the axial geometry. When in focus, the field of view of the spectrometer is filled out to a range of 340 cm. The solid angle of the Imaging Spectrometer is $3 \times 10^{-5} \text{ sr}$. When viewing the near field with optics focused at infinity, the Imaging Spectrometer slit is over filled out to a range of 300 cm and the area of the

incident beam is the limiting factor when evaluating the integral over the object plane. Table II lists the effective fields of view for several ranges. The out-of-focus sensitivity is approximately 30% of the in-focus sensitivity for this geometry.

The in-focus and out-of-focus sensitivities are nearly equivalent; however, the imaging properties of the spectrometer are sacrificed in the out-of-focus case. Since the object is focused behind the slit in the out-of-focus case, the spectral resolution of the instrument also will be affected.

2.3.4 Comparison of Axial and Perpendicular Geometries

In order to increase the length of the line-of-sight integration path through a radiating region, the detector can be placed such that its field of view is aligned with the incident beam (see Figure 9). The distance at which the field of view of the detector is exactly filled by the incident beam is given by r_e . For a circular field of view, r_e is given by

$$r_e = \left(\frac{\pi w^2}{4\Omega} \right)^{1/2}$$

where w is the diameter of the incident beam and Ω is the solid angle of the detector. For an elliptic field of view r_e is given by

$$r_e = \frac{w}{2 \sin(\Theta/2)}$$

where Θ is the angular field of view in one direction.

Given the incident beam diameter of six centimeters, r_e for the Krypton Radiometer is 24 cm. The field of view of the Imaging Spectrometer is $1^\circ \times 0.1^\circ$. In the 1° direction, r_e is 340 cm, while in the 0.1° direction r_e is 3400 cm. A mean value for r_e of 960 cm is calculated by using the solid angle of 3×10^{-5} sr for the Imaging Spectrometer.

Ignoring the effect of being out of focus, the differential signal is given by

$$dS = \beta \cdot A_{te1} \cdot \rho(r) \cdot \frac{dv}{(r-r_o)^2}$$

Table II

Out of Focus Sensitivities for the APL Imaging Spectrometer.

A 6 cm Diameter Incident Beam is Used in the Axial Geometry.

Q is the Fraction of the Blur Circle which Passes Through the Slit.

The Integral is the effective field of view.

For Ranges out to 340 cm, the Out of Focus Sensitivity is
30% of the Infocus Sensitivity.

Range (cm)	Q	$\int Q \cdot \frac{dA_0}{r^2}$
30	2.80E-04	8.80E-06
40	4.97E-04	8.80E-06
50	7.77E-04	8.80E-06
60	1.12E-03	8.80E-06
70	1.52E-03	8.80E-06
80	1.99E-03	8.80E-06
90	2.52E-03	8.80E-06
100	3.11E-03	8.80E-06
110	3.76E-03	8.80E-06
120	4.48E-03	8.60E-06
130	5.25E-03	8.80E-06
140	6.09E-03	8.80E-06
150	6.99E-03	8.80E-06
160	7.96E-03	8.80E-06
170	8.98E-03	8.80E-06
180	1.01E-02	8.80E-06
190	1.12E-02	8.80E-06
200	1.24E-02	8.80E-06
210	1.37E-02	8.80E-06
220	1.50E-02	8.80E-06
230	1.64E-02	8.80E-06
240	1.79E-02	8.80E-06
250	1.94E-02	8.80E-06
260	2.10E-02	8.80E-06
270	2.27E-02	8.80E-06
280	2.44E-02	8.80E-06
290	2.61E-02	8.80E-06
300	2.80E-02	8.80E-06
310	2.99E-02	8.80E-06
320	3.18E-02	8.80E-06
330	3.39E-02	8.80E-06
340	3.59E-02	8.80E-06



Figure 9. Axial and perpendicular geometries. w is the diameter of the incident beam, r_e is the distance at which the beam exactly fills the field of view.

$$\beta = \frac{1}{4\pi} f \cdot \sigma_{pe} \cdot \eta \cdot T \cdot R_d$$

where A_{tel} is the area of the collection optics expressed in cm^2 , $r-r_c$ is the distance from dV to the collection optics, f is the incident flux expressed in photons $\text{cm}^{-2}\text{sec}^{-1}$, σ_{pe} is the photoemission cross-section expressed in cm^2 molecule $^{-1}$, η is the detector quantum efficiency, T is the filter transmission, and R_d is the duty cycle. The H_2O density, $\rho(r)$ is given by

$$\rho(r) = \rho_o \cdot \left(\frac{r_o}{r} \right)^2$$

where ρ_o is the density near the surface of the spacecraft and r_o is the characteristic dimension of the spacecraft. The characteristic dimension is chosen as 240 cm (half the length of the spacecraft). In the axial geometry, the volume element, dV , is given by

$$\text{for } r < r_e + r_o \quad dV = \Omega \cdot (r-r_o)^2 dr$$

$$\text{for } r > r_e + r_o \quad dV = \frac{\pi w^2}{4} \cdot dr$$

The signal is given by

$$S = \beta \cdot A_{tel} \int_{r_o}^{r_o + r_e} \rho_o \left(\frac{r_o}{r} \right)^2 \Omega (r-r_o)^2 \frac{dr}{(r-r_c)^2} t \times$$

$$+ \beta \cdot A_{tel} \int_{r_o + r_e}^{\infty} \rho_o \left(\frac{r_o}{r} \right)^2 \frac{\pi w^2}{4} \frac{dr}{(r-r_o)^2}$$

Evaluation of this integral yields

$$S = \beta \cdot A_{tel} \cdot \rho_o \left[\Omega r_o^2 \left(\frac{1}{r_o} - \frac{1}{r_o + r_e} \right) + \frac{\pi w^2}{4} \left[\frac{2r_e + r_o}{r_e (r_e + r_o)} + \frac{2}{r_o} \ln \left(\frac{r_e}{r_e + r_o} \right) \right] \right].$$

If r_e is taken to be the mean value of 960 cm, the signal in the axial geometry is then

$$S = \beta \cdot A_{tel} \cdot \rho_o \cdot [5.3 \times 10^{-3}]$$

In the perpendicular geometry, assuming the field of view is full, the volume element is given by

$$dV = \Omega \cdot (r - r_o)^2 dr$$

The signal is given by

$$S = \beta \cdot A_{tel} \int_{R_{min}}^{R_{max}} \rho_o \left(\frac{r_o}{r} \right)^2 \Omega (r - r_o)^2 \frac{dr}{(r - r_o)^2}$$

$$S = \beta \cdot A_{tel} \cdot \rho_o \cdot r_o^2 \cdot \Omega \frac{w}{R_{max} \cdot R_{min}}$$

For a small diameter beam in the near field, $R_{max} \sim R_{min} \sim r_o$, and the signal is given approximately by

$$S \sim \beta \cdot A_{tel} \cdot \rho_o \cdot \Omega \cdot w$$

Evaluation of this expression for the Imaging Spectrometer yields

$$S \sim \beta \cdot A_{tel} \cdot \rho_0 (1.8 \times 10^{-4})$$

Thus there is a thirty-fold advantage for using the Imaging Spectrometer in the axial geometry, rather than in the perpendicular geometry.

This same type of analysis can also be performed for the Krypton Radiometer. The results are summarized in Table III. Assuming similar quantum efficiencies for the two detectors, the Krypton Radiometer, when used in the perpendicular geometry, is fourteen times as sensitive as the Imaging Spectrometer used in the axial geometry.

2.4 Existing Measurements of Spaceborne H₂O Concentration

Previous space shuttle missions have carried particulate and gaseous contamination experiments^[8-12]. The gaseous contamination measurements were performed using mass-spectrometric and infrared spectroscopic techniques. The different measurement techniques yield different measures of the concentration, e.g., column densities, near-field densities and outgassing rates. Some assumptions about the vehicle must be made in order to compare the different results.

The surface flux expressed in molecules cm⁻² sec⁻¹ is given by

$$f_{surf} = \frac{m \cdot N_A}{M \cdot A}$$

where m is the outgassing rate in grams sec⁻¹, N_A is Avogadro's number, M is the molecular weight of the species and A is the surface area of the vehicle. The near-field density expressed in molecules cm⁻³ is given by

$$\rho = \frac{2 \cdot f_{surf}}{v}$$

Table III

Sensitivities of the Krypton Radiometer and the APL Imaging Spectrometer in the Axial and Perpendicular Geometries

	Signal (Counts Sec ⁻¹)	
	<u>Axial</u>	<u>Perpendicular</u>
Krypton Radiometer	27 β_{p_0}	7.5 β_{p_0}
Imaging Spectrometer	0.53 β_{p_0}	0.018 β_{p_0}

$$\beta = f \cdot \sigma_{pe} \cdot \eta \cdot T \cdot R \cdot \frac{1}{4\pi}$$

where v is the average thermal velocity of 5×10^4 cm sec⁻¹. The column density, D_c , is given by

$$D_c(r_b) = \int_{r_b}^{R_{max}} \rho(r) dr$$

For a cylindrical object, the local density, $\rho(r)$, falls off roughly as the distance from the body

$$\rho(r) = \rho(r_b) \cdot \left(\frac{r_b}{r} \right)$$

where r_b is the radius of the body and $\rho(r_b)$ is the local density at the surface of the body. The column density is then given by

$$D_c(r_b) = \rho(r_b) \cdot r_b \cdot \ln \frac{R_{max}}{r_b}$$

To the extent that the space shuttle can be approximated by a cylinder roughly 4.6 meters in diameter and 36 meters in length, we can compare the various concentration measurements. R_{max} is the shuttle length and r_b is the shuttle radius.

Data from an infrared telescope flown on Spacelab-2 indicate a column density of $1 \times 10^{13} - 1 \times 10^{14}$ molecules cm⁻²^[11]. Given the shuttle radius of 2.3 meters, we find that this column density is equivalent to a near-field density of $1.6 \times 10^{10} - 1.6 \times 10^{11}$ molecules cm⁻³.

Mass-spectrometric data obtained during STS-41C, indicate a near-field density of $1 \times 10^8 - 2 \times 10^9$ molecules cm⁻³^[12]. Other mass-spectrometric data obtained during STS-2,3,4,9 indicate quiescent column densities of $4 \times 10^{10} - 3 \times 10^{12}^[8]. These values are equivalent to near field densities of $6.3 \times 10^7 - 4.7 \times 10^9$ molecules cm⁻³. These results are summarized in Table IV.$

Table IV
Previously Measured Spaceborne Water Vapor Concentrations

<u>Mission</u>	<u>Technique</u>	$\underline{F}_{surf} (\text{cm}^{-2} \text{s}^{-1})$	$\underline{\rho}_o (\text{cm}^{-3})$	$\underline{D}_c (\text{cm}^{-2})$
Spacelab 2	Infrared Telescope	$4 \times 10^{14} -$ 4×10^{15}	$1.6 \times 10^{10} -$ 1.6×10^{11}	$10^{13} - 10^{14} *$
STS 2,3,4,9	Mass Spectrometer	$1.6 \times 10^{12} -$ 1.2×10^{14}	$6.3 \times 10^7 -$ 4.7×10^9	$4 \times 10^{10} -$ 3×10^{12}
STS-41C	Mass Spectrometer	$2.5 \times 10^{12} -$ 5.0×10^{13}	$1 \times 10^8 - *$ 2×10^9	$6.2 \times 10^{10} -$ 1.2×10^{12}

* Indicates Measured Value

2.5 Calculations of Expected Signal Levels

2.5.1 Derivation of Signal/Noise Expression for the Krypton Radiometer

The Krypton Radiometer is shown schematically in Figures 7a-b. Under optically thin conditions, the number of electronically excited OH radicals produced per cubic centimeter per second is given by

$$[\text{OH}^*] = f \cdot \sigma_{pe} \cdot [\text{H}_2\text{O}]$$

where f is the incident 1236 Å flux expressed in photons $\text{cm}^{-2} \text{sec}^{-1}$, $[\text{H}_2\text{O}]$ is the H_2O concentration expressed in molecules cm^{-3} and σ_{pe} is the photoemission cross-section expressed in $\text{cm}^2 \text{molecule}^{-1}$. Recall that the photoemission cross-section is equal to the H_2O absorption cross-section multiplied by the efficiency for the production of electronically excited OH radicals.

$$\sigma_{pe} = \sigma_{abs} \cdot \phi^*$$

The number of photoelectrons created per second at the PMT photocathode by the collected OH emission is given by

$$S = f \cdot \sigma_{pe} \cdot [\text{H}_2\text{O}] \cdot \frac{A \cdot \Omega}{4\pi} \cdot w \cdot \eta \cdot T \cdot t \cdot x$$

where S is the signal expressed in counts sec^{-1} , A is the area of the collection optics expressed in cm^2 , Ω is the solid angle of the detector field of view expressed in steradians, w is the diameter of the incident beam expressed in cm, η is the quantum efficiency of the detector and T is the filter transmission. The solid angle of the detector is given by

$$\Omega = \frac{\pi d^2}{4 r^2}$$

where d for the Krypton Radiometer is the diameter of the PMT photocathode and r is the distance of the irradiated region from the detector optics. Ω is equal to 0.05 sr for this system.

The signal obtained after integration for a time t is given by

$$S(t) = S \cdot R_d \cdot t$$

$$S(t) = 4.18 \times 10^{-20} \cdot f \cdot [H_2O] \cdot t$$

where R_d is the duty cycle of the lamp and is equal to 0.5.

Several sources of noise will be present in the water vapor contamination measurement. Among them are the noise from the dark current of the photomultiplier tube, the noise from the celestial background, the noise from the photolysis of H_2O vapor by solar radiation and noise due to Rayleigh scattering of solar radiation.

The noise obtained from the PMT dark current after an integration for a time t is given by

$$N(t) = (D \cdot (1-R_d) \cdot t)^{1/2}$$

where D is the dark current of 14 counts per second at 293° K and R is the duty cycle of the lamp. Evaluation of this expression yields

$$N_{\text{dark}} = 2.65 \cdot t^{1/2}$$

This value can be reduced by cooling the PMT.

The noise due to the celestial background after an integration for a time t is given by

$$N(t) = (B_c \cdot A \cdot \Omega \cdot \Delta\lambda \cdot \frac{\lambda}{hc} \cdot \eta \cdot T \cdot (1-R_d) \cdot t)^{1/2}$$

where B_c is the celestial spectral radiance of 1×10^{-10} Watts m^{-2} deg^{-2} μm^{-1} at 3000 Å when looking perpendicular to the galactic plane⁽¹²⁾. Evaluation of this expression yields

$$N_{\text{celest}} = 180 \cdot t^{1/2}$$

The noise due to photolysis of the H_2O by incident VUV solar flux and subsequent OH emission is given by

$$N(t) = \left[f_{\text{solar}} \cdot \sigma_{\text{pe}} \cdot [H_2O] \cdot \frac{A \cdot \Omega}{4\pi} \cdot w \cdot \eta \cdot T \cdot (1-R_d) \cdot t \right]^{1/2}$$

where f_{solar} is the incident VUV solar flux of 2.6×10^{11} photons $\text{cm}^{-2} \text{sec}^{-1}$. The two meter spacecraft diameter is used for the path length, w , since the density falls with the square of the distance. Evaluation of this expression yields

$$N_{\text{solar}} = 4.26 \times 10^{-4} \cdot [H_2O]^{1/2} \cdot t^{1/2}$$

The noise due to Rayleigh scattering of incident solar radiation after an integration for time t is given by

$$N(t) = \left[f_{\text{solar}} \cdot \sigma_{\text{ray}} \cdot n_{\text{tot}} \cdot \frac{A \cdot \Omega}{4\pi} \cdot w \cdot \eta \cdot T \cdot (1-R_d) \cdot t \right]^{1/2}$$

where σ_{ray} is the Rayleigh scattering cross-section of $5.6 \times 10^{-26} \text{ cm}^2 \text{ molecule}^{-1}$, f_{solar} is the incident 3000 - 3200 Å solar flux of 1.5×10^{15} photons $\text{cm}^{-2} \text{sec}^{-1}$ and n_{tot} is the total atmospheric density expressed in molecules cm^{-3} . The ambient density at an altitude of 880 km is 1.3×10^5 molecules cm^{-3} . The spaceborne H_2O concentration may be much greater than the total ambient density. Evaluation of this expression yields.

$$N_{\text{RAY}} = 6.54 \times 10^{-6} \cdot n_{\text{tot}} \cdot t^{1/2}$$

The 1236 Å output power of the modified lamp discussed in section 2.3.1 is 8×10^{15} photons sec^{-1} . Assuming that half of the output power is collimated into a 6 cm diameter beam, we find that the incident flux is 1.4×10^{14} photons $\text{cm}^{-2} \text{sec}^{-1}$. Comparisons of the signal level, obtained with this incident flux, to the various noise levels are summarized in Figures 10a-b for one second and 100 second integration times.

Krypton Radiometer 1 sec. integration

90-356

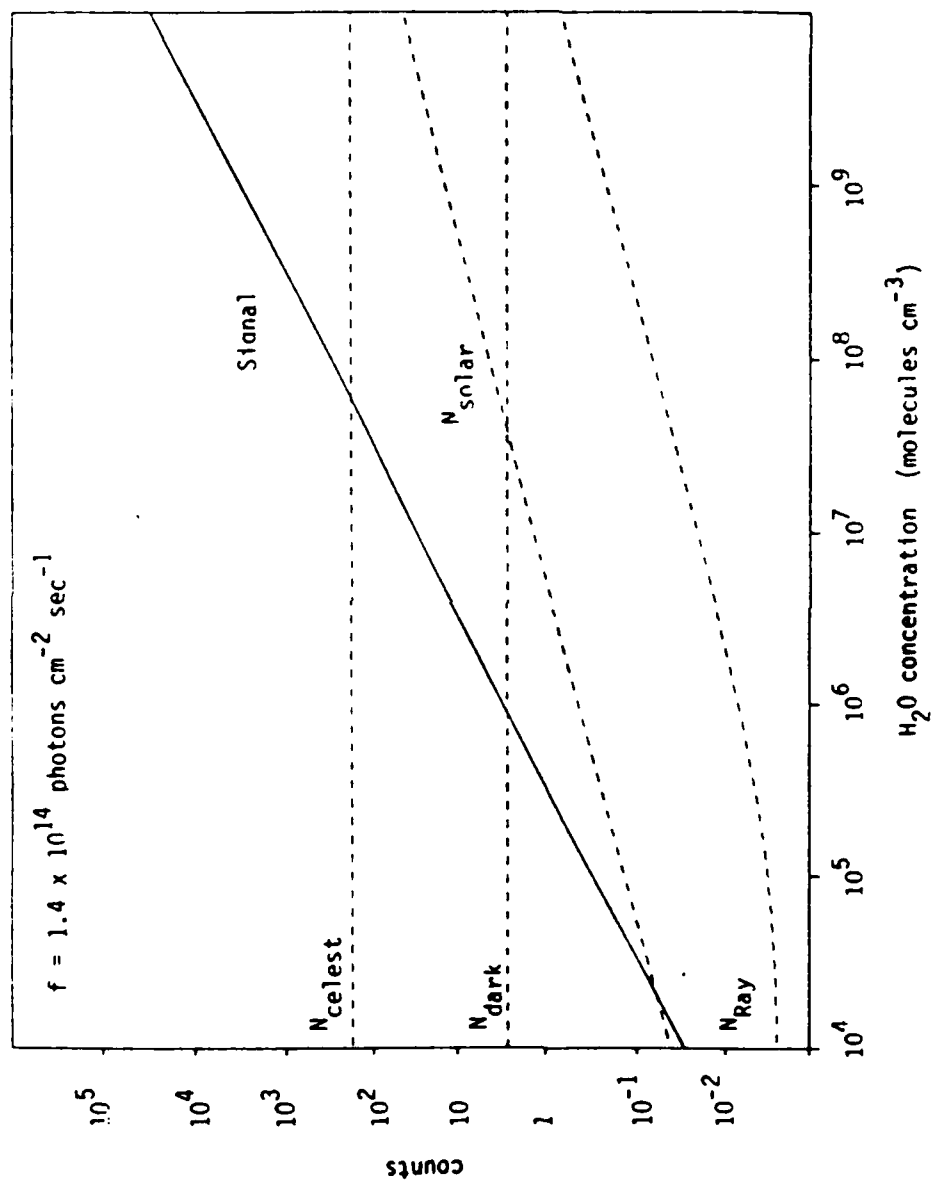


Figure 10a. OH photoemission signal and several sources of noise for a one second integration time for the small radiometer. N_{dark} is the noise due to the PMT dark current, N_{celest} is the noise due to the celestial background, N_{Ray} is the noise due to Rayleigh scattering of solar radiation, N_{solar} is the noise due to photoemission caused by the incident VUV solar radiation.

Krypton Radiometer 100 sec. integration

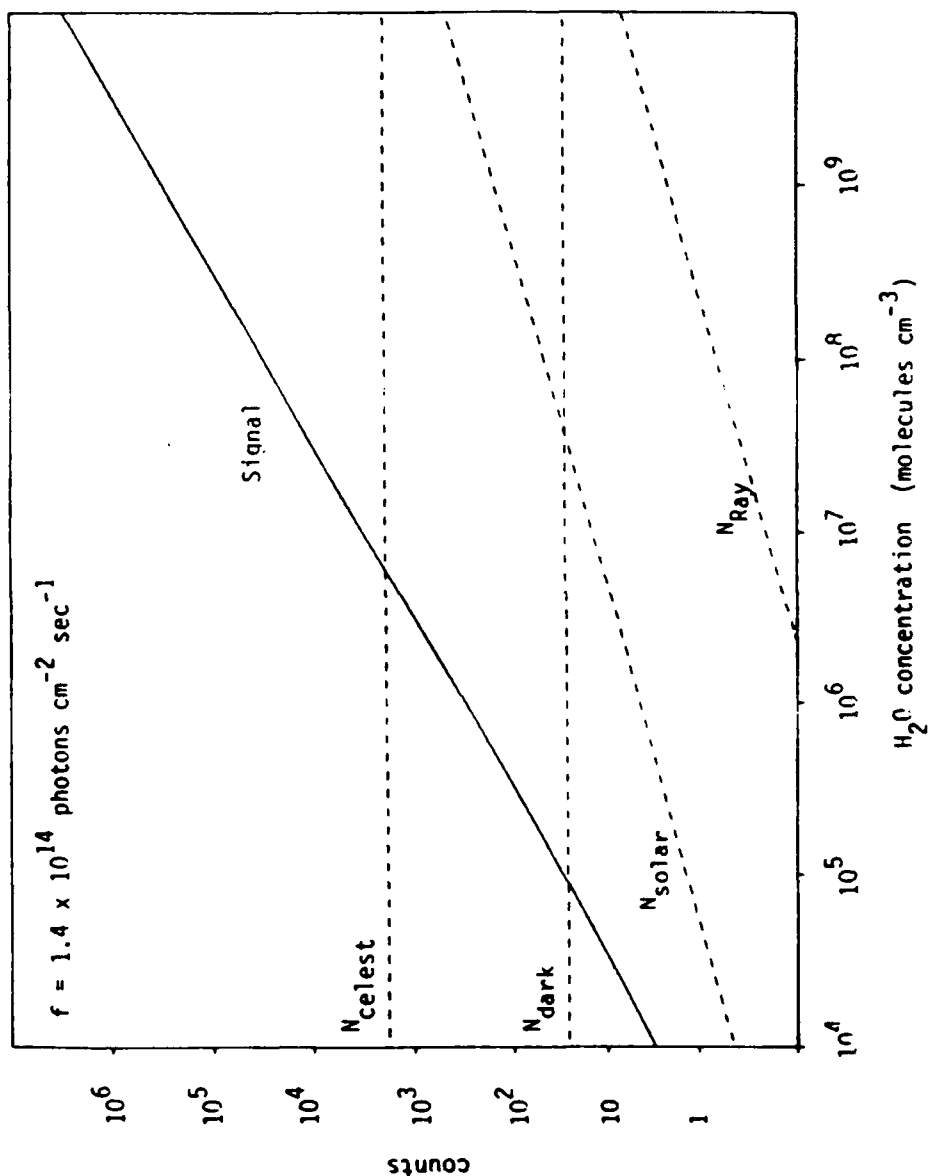


Figure 10b. OH photoemission signal and several sources of noise for a 100 second integration time for the small radiometer. N_{dark} is the noise due to the PMT dark current, N_{celest} is the noise due to the celestial background, N_{Ray} is the noise due to Rayleigh scattering of solar radiation, N_{solar} is the noise due to photoemission caused by the incident VUV solar radiation.

The dominant noise term is that from the celestial background. For a one second integration time, the minimum detectable H_2O concentration (with $S/N = 1$) is 6×10^7 molecules cm^{-3} and for a 100 second integration time $[\text{H}_2\text{O}]_{\min}$ is 6×10^6 molecules cm^{-3} .

If the celestial background can be blocked (see Figure 7b), the dominant noise term becomes that from the PMT dark current. In this case the minimum detectable H_2O concentration is 9×10^5 molecules cm^{-3} for a one second integration and 9×10^4 molecules cm^{-3} for a 100 second integration.

2.5.2 Fractional Dissociation

In order to decrease the minimum detectable H_2O concentration, the incident VUV flux can be increased. For a given concentration, however, there is no point in increasing the flux if the ambient H_2O concentration is already significantly depleted.

The fraction of H_2O molecules dissociated in a time, t_r , is given by

$$\text{Fractional Dissociation} = 1 - \exp [-f \cdot \sigma_{abs} \cdot t_r]$$

where f is the incident VUV flux expressed in photons $\text{cm}^{-2} \text{sec}^{-1}$, and σ_{abs} is the water vapor absorption cross-section expressed in $\text{cm}^2 \text{molecule}^{-1}$.

The average residence time of an H_2O molecule in the detectable region is given by

$$t_r = \frac{w}{v}$$

where v is the average thermal velocity of 5×10^4 cm sec^{-1} and w is diameter of the irradiated region. The probability of being dissociated, or the fractional dissociation, is then given by

$$\text{fractional dissociation} = 1 - \exp \left[\frac{-f \cdot \sigma_{abs} \cdot w}{v} \right]$$

The fractional dissociation as a function of incident flux is shown in Figure 11. For the fluxes of interest the fractional dissociation is negligible.

Fractional Dissociation of Water Vapor

90-358

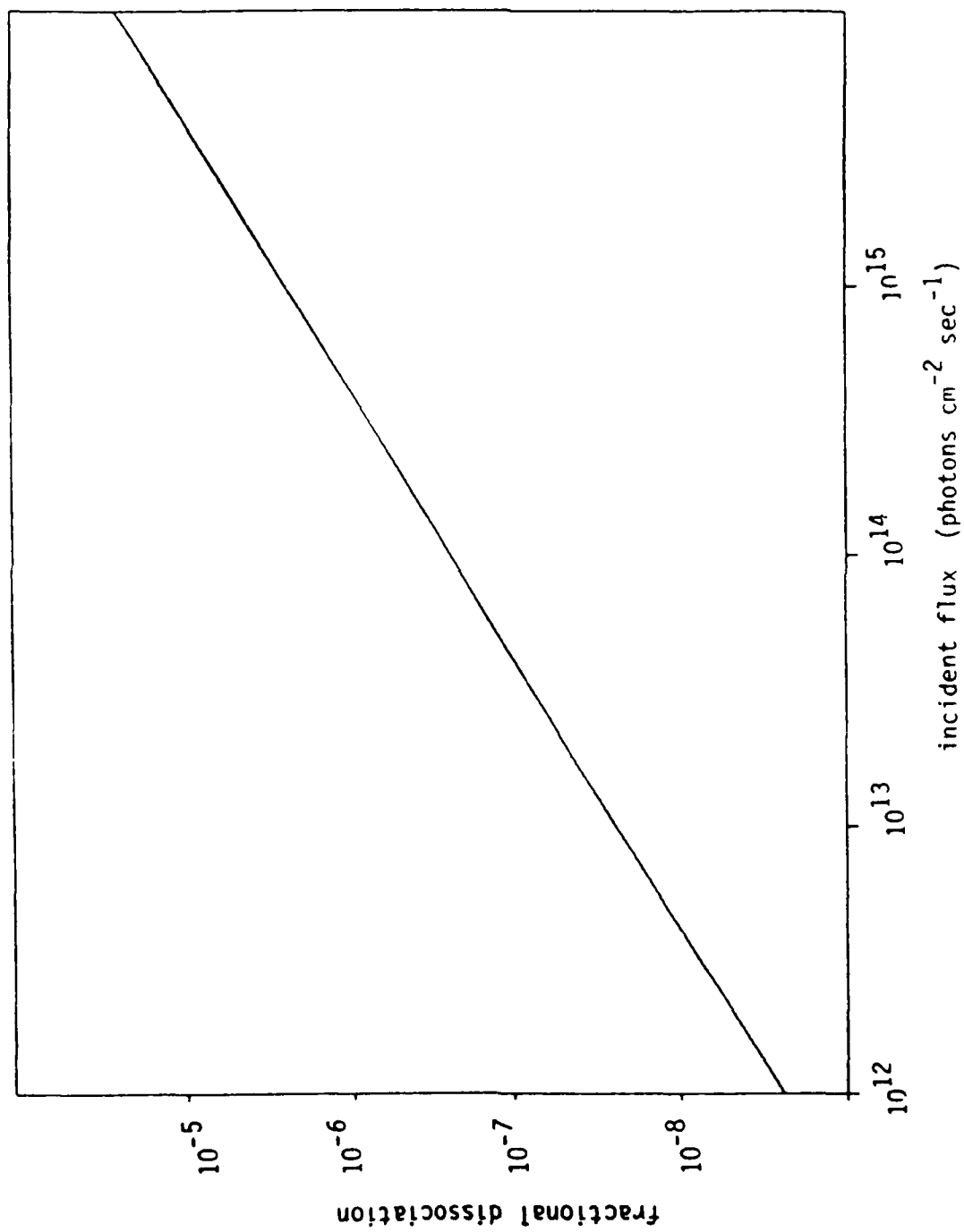


Figure 11. Fractional dissociation of H_2O as a function of incident flux.

2.6 Preliminary Flight Specifications

A preliminary estimate of the engineering specifications for the water vapor contamination experiment is given in Table V. The Krypton Radiometer and power supplies will occupy a box roughly 5 x 10 x 16 inches and will weigh approximately 19.5 pounds. The average input power will be 60 W. Some external optics will be required, specifically a turning mirror, focusing optics, a filter, and a retro-reflector. The data requirements are also given in Table V. Eight bit resolution on various monitoring channels is required. Specifically, the power supply electrical properties, the power supply temperature and the VUV flux must be monitored.

2.7 Topics Requiring Further Study

Several items require further study before implementation of the experiment. The krypton lamp and power supply prototype must be fabricated and tested to determine the actual VUV flux, input power requirements, cooling requirements and the expected lifetime of the system. Finally, the actual experimental payload must be designed and reviewed.

Table V

Preliminary Engineering Specifications for the Krypton Radiometer

Weight	19.5 lbs.	
Size	5 in. x 10 in. x 16 in.	
Power (Avg)	60 W	
Data Requirements (Power Supply)	Samples/Sec	Resolution (Bits)
28 VDC Voltage Monitor	<1	8
Source Voltage Monitor	4	8
Source Current Monitor	4	8
Power Supply Temperature Monitor	<1	8
Source UV Flux Monitor	20	8
Data Requirements (Detector)		
28 VDC Voltage Monitor	1	8
HV Monitor 1	1	8
HV Monitor 2	1	8
Temp Monitor	1	8
Sensor Counts	20	16
Controls		
Source On/Off		
Pulse Synchronization		
Detector On/Off		
Detector Test		

3. MEASUREMENT OF PARTICULATE CONCENTRATION

3.1 Particulate Scattering Phenomenology - Mie Scattering

The interaction of an incident plane wave propagating through a medium of a given refractive index with a spherical particle having a different refractive index is well described, in general, by the familiar theory developed by Mie^[14]. The intensity of the scattered radiation and its angular properties depend upon the wavelength of the incident radiation, the refractive index of the particulate matter and the size of the particle.

By irradiating the near field with visible radiation ($0.5 \mu\text{m}$) and observing the scattered radiation occurring at the incident wavelength, particulate matter which is present can be detected. The size, number, and distance of the particles determine the intensity of the scattered radiation, while the velocity of the particles determines how they will be tracked by the detector.

3.2 Conceptual Design of the Experiment

A conceptual drawing of the experiment is shown in Figure 12. The output of a pulsed xenon arc lamp is collimated by a parabolic reflector into a beam. Scattered radiation is detected either axially or at right angles to the incident beam with the onboard APL imager. The active volume is assumed to fill the field of view of the detector.

3.3 Experimental Apparatus

3.3.1 Xenon Lamp

The incident radiation source under consideration is a 500 Watt xenon short arc lamp having a pulse width of 10 msec. The maximum repetition rate depends upon the cooling requirements of the lamp. Several equivalent lamps are commercially available. (The spectral irradiance of a xenon arc lamp is shown in Figure 13.) The spectral power output of the lamp is constant through most of the visible region at 0.16 W nm^{-1} ^[15]. If 50% of the lamp output power in a 100 nm band centered at 500 nm is collimated into beam, the incident power is then $2 \times 10^{19} \text{ photons sec}^{-1}$.

3.3.2 Detector

Two onboard APL Imagers are available for use as the detector in the particulate contamination experiment^[1]. The first is the narrow field of view

PARTICLE CONTAMINATION MEASUREMENT CONCEPTUAL GEOMETRY

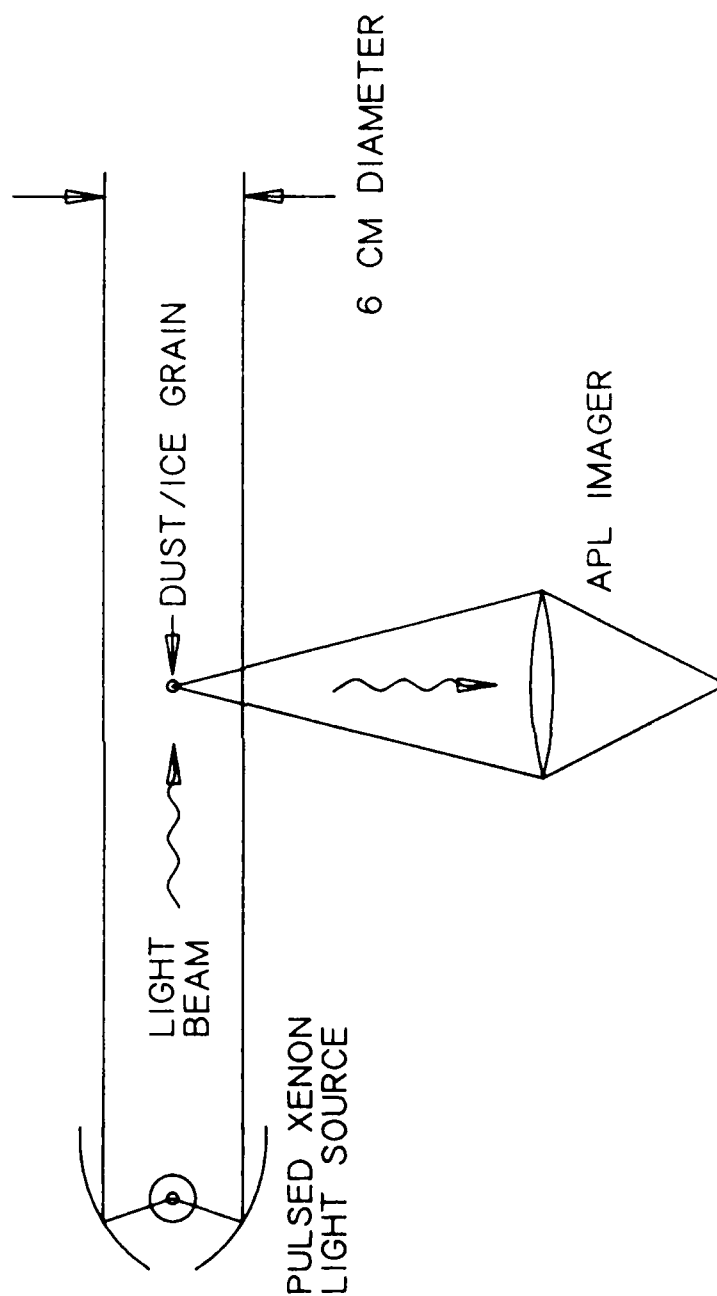


Figure 12. Conceptual drawing of the particulate contamination experiment. The experiment can be performed in either the perpendicular geometry (as shown) or in the axial geometry (detecting along the incident beam).

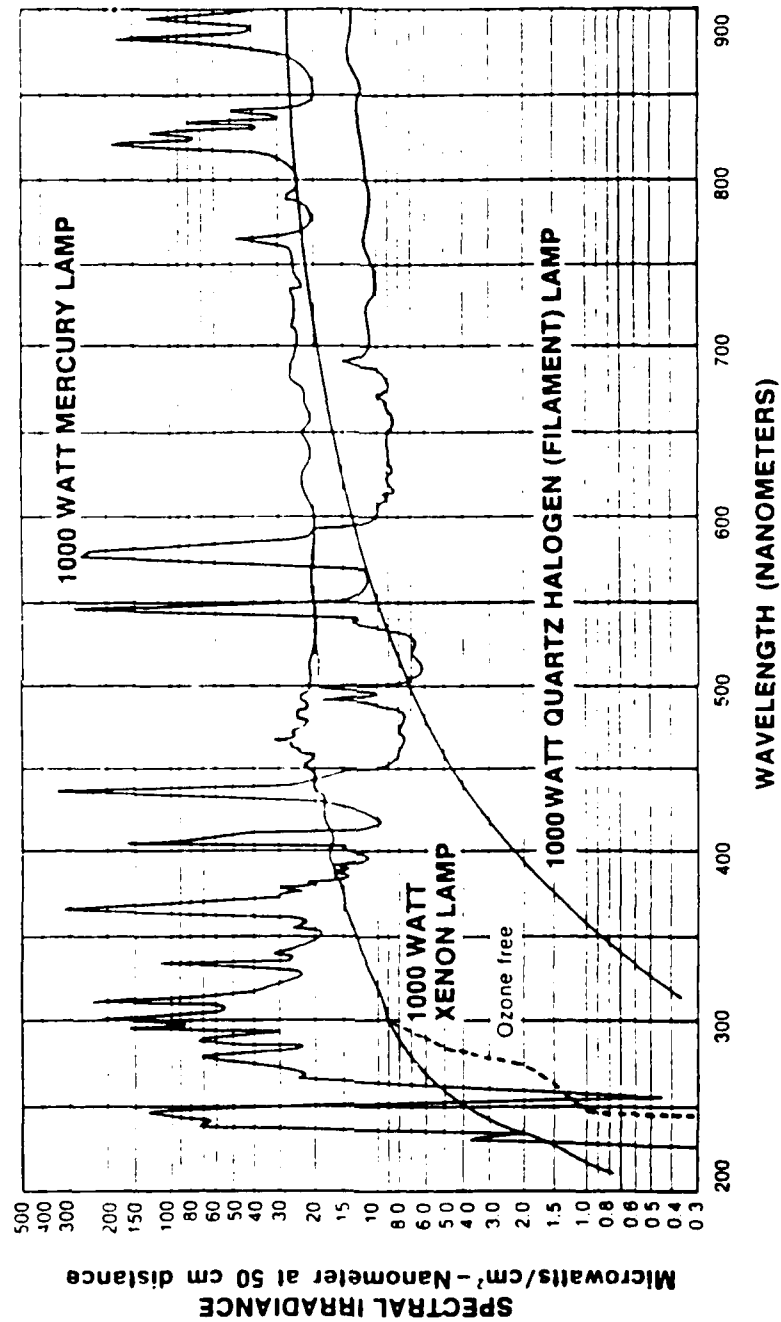


Figure 13. Spectral irradiance from a 1000 W xenon flashlamp. The flash-lamp proposed for the Xenon Unit is a 500 W xenon short arc lamp.

(NFOV) Imager. It consists of a 150 x 170 pixel array with collection optics focused at infinity. Each pixel corresponds to a field of view of 0.01 x 0.01 degrees. The sensitivity for this array is 100 Rayleighs. The collection optics have an area of 100 cm².

The second detector is the wide field of view (WFOV) Imager. It is also a 150 x 170 pixel array with collection optics focused at infinity. The field of view of each pixel is 0.1 x 0.1 degree. The area of the collection optics is 25 cm².

3.3.3 Detector Optics

Modification of the collection optics for the APL WFOV Imager can be provided to allow focusing in the near field. The modification would include the addition of a lens set to allow focusing at the center of the irradiated region. No modification of APL NFOV Imager collection optics can be provided.

3.4 Existing Measurements of Spaceborne Particulate Contamination

As mentioned in section 2.4 several measurements of particulate contamination have been made. Koch et al.^[11] state the STS Contamination Control Requirement for particulate matter as one detectable particle per orbit per 1.5×10^{-5} sr. A detectable particle is defined as particle with a radius of at least 5 μm , within a range of 10 km. Given an orbital time of approximately 1.5 hours, the particle detection frequency requirement becomes 12 sec⁻¹ sr⁻¹.

A Skylab experiment (1973) using video cameras, measured particles as small as 5 μm and observed an $r^{-1.5}$ size distribution. Velocities ranged from 0.1 - 20 meters sec⁻¹ with larger particles moving more slowly^[9].

A temperature controlled quartz crystal microbalance experiment was flown on Spacelab 1. These measurements indicate that most of the particles are in the 1 - 20 μm range. Also, the sensor facing out of the bay accumulated the least mass, indicating that collisional backscattering of particles is not significant^[11].

The induced environment contamination monitor (IECM) experiments were flown on STS 2,3,4 and 9^[8,10]. One experiment consisted of a 32 degree FOV stereo camera/photometer system with a range of 50 meters used to observe solar scattering from particles. One 25 μm particle per one degree FOV per three

hours is reported, or $0.39 \text{ particles sec}^{-1} \text{ sr}^{-1}$. The lowest detectable particle size is $25 \mu\text{m}$. Forty-two percent of the particles were less than $40 \mu\text{m}$ in diameter and the average velocity of the particles was 1.2 m sec^{-1} .

An infrared telescope having a 0.6×1.0 degree FOV and a range of 20 meters was flown on STS-51F^[11]. Forty-three particles between 70 and $265 \mu\text{m}$ were detected in a ten minute period with this instrument. This corresponds to $390 \text{ sec}^{-1} \text{ sr}^{-1}$.

A 17×24 degree FOV stereo camera system was flown on STS-61C^[9]. This system could detect particles as small as $30 \mu\text{m}$. The camera was focused at 25 m and was equipped with a 25 W xenon flashlamp to allow nighttime measurements of the particulate contamination, although the majority of data were obtained under sunlit conditions. One particle per second was detected in the field of view, or eight particles $\text{sec}^{-1} \text{ sr}^{-1}$. These previous measurements are summarized in Table VI.

All reports indicate that terminator crossings are important in the release of particulate matter from the spacecraft as well as water dumps and thruster firings. Clifton and Owens^[10] also indicate that after approximately 15 hours mission elapsed time (MET) a fairly quiescent rate of particulate release is achieved except for the instances mentioned above. Green, et. al indicate that peak detection rates are approximately 15X greater than average rates^[9].

3.5 Calculation of Mie Scattering Cross-sections

Under optically thin conditions where multiple scattering effects are unimportant, the differential scattering cross-sections for the particle sizes described in the previous section can be calculated using Mie theory^[14]. The partial differential scattering cross-section is given by

$$\frac{d\sigma}{d\Omega} = \frac{1}{2k^2} \left[|S_1(\Theta)|^2 + |S_2(\Theta)|^2 \right]$$

where $k = 2\pi/\lambda$ and $S_1(\Theta)$ and $S_2(\Theta)$ are given by

$$S_1(\Theta) = \sum_{n=1}^{\infty} \frac{2n+1}{n(n+1)} \left[a_n \pi_n(\cos\Theta) + b_n \tau_n(\cos\Theta) \right]$$

Table VI
Previously Measured Spaceborne Particulate Detection Rates

<u>Mission</u>	<u>Detector</u>	<u>FOV</u>	<u>Min Part Size</u>	<u>Range</u>	<u>Rate</u>
*CCR	N/A	$1.5 \times 10^{-5} \text{ sr}$	$5 \text{ } \mu\text{m}$	10 Km	$12 \text{ s}^{-2} \text{ sr}^{-1}$
STS2-4,9	Stereo Camera	32°	$25 \text{ } \mu\text{m}$	50 M	$0.39 \text{ s}^{-1} \text{ sr}^{-1}$
STS-51F	IR Telescope	$1.0 \times 0.6^\circ$	$70 \text{ } \mu\text{m}$	20 M	$390 \text{ s}^{-1} \text{ sr}$
STS-61C	Stereo Camera	$17 \times 24^\circ$	$30 \text{ } \mu\text{m}$	25 M	$8 \text{ s}^{-1} \text{ sr}^{-1}$

- Particle Size Distribution $\cdot r^{-1.5}$

- Velocities $10 \text{ cm s}^{-1} - 2000 \text{ cm s}^{-1}$

$$S_1(\Theta) = \sum_{n=1}^{\infty} \frac{2n+1}{n(n+1)} \left[b_n \pi_n(\cos\Theta) + a_n \tau_n(\cos\Theta) \right]$$

π_n and τ_n are functions of the associated Legendre functions, $P_n^1(\cos\Theta)$, and are given by

$$\pi_n = \frac{1}{\sin\Theta} P_n^1(\cos\Theta)$$

$$\tau_n = \frac{d}{d\Theta} P_n^1(\cos\Theta)$$

a_n and b_n are functions of the Ricatti-Bessel functions, $\Psi_n(z)$, $\chi_n(z)$ and $\zeta_n(z)$, and are given by

$$a_n = \frac{\Psi'_n(Y)\Psi_n(x) - m\Psi_n(Y)\Psi'_n(x)}{\Psi'_n(Y)\zeta_n(x) - m\Psi_n(Y)\zeta'_n(x)}$$

$$b_n = \frac{\Psi'_n(Y)\Psi_n(x) - m\Psi_n(Y)\Psi'_n(x)}{\Psi'_n(Y)\zeta_n(x) - m\Psi_n(Y)\zeta'_n(x)}$$

where $x = 2\pi a/\lambda$, a is the particle radius, $y = mx$ and m is the complex refractive index. Using a computer code, the Mie scattering cross-sections are easily calculated. The results of the calculation for $\Theta = 90$ degrees, $\lambda = 0.5 \mu\text{m}$ and various particle sizes are given in Table VII. Figures 14a-b illustrate the angular dependence of the differential scattering cross-section for several particle sizes.

Table VII

Differential Scattering Cross-Sections for Various Size Spherical
Ice Particles for 5000 Å Radiation and 90° Geometry

Mie Scattering

Particle Radius μm	$\frac{d\sigma}{d\Omega}$ cm^2/sr
0.30	6.68×10^{-11}
0.50	2.16×10^{-10}
1.00	3.97×10^{-10}
3.00	3.88×10^{-9}
10.0	9.41×10^{-9}

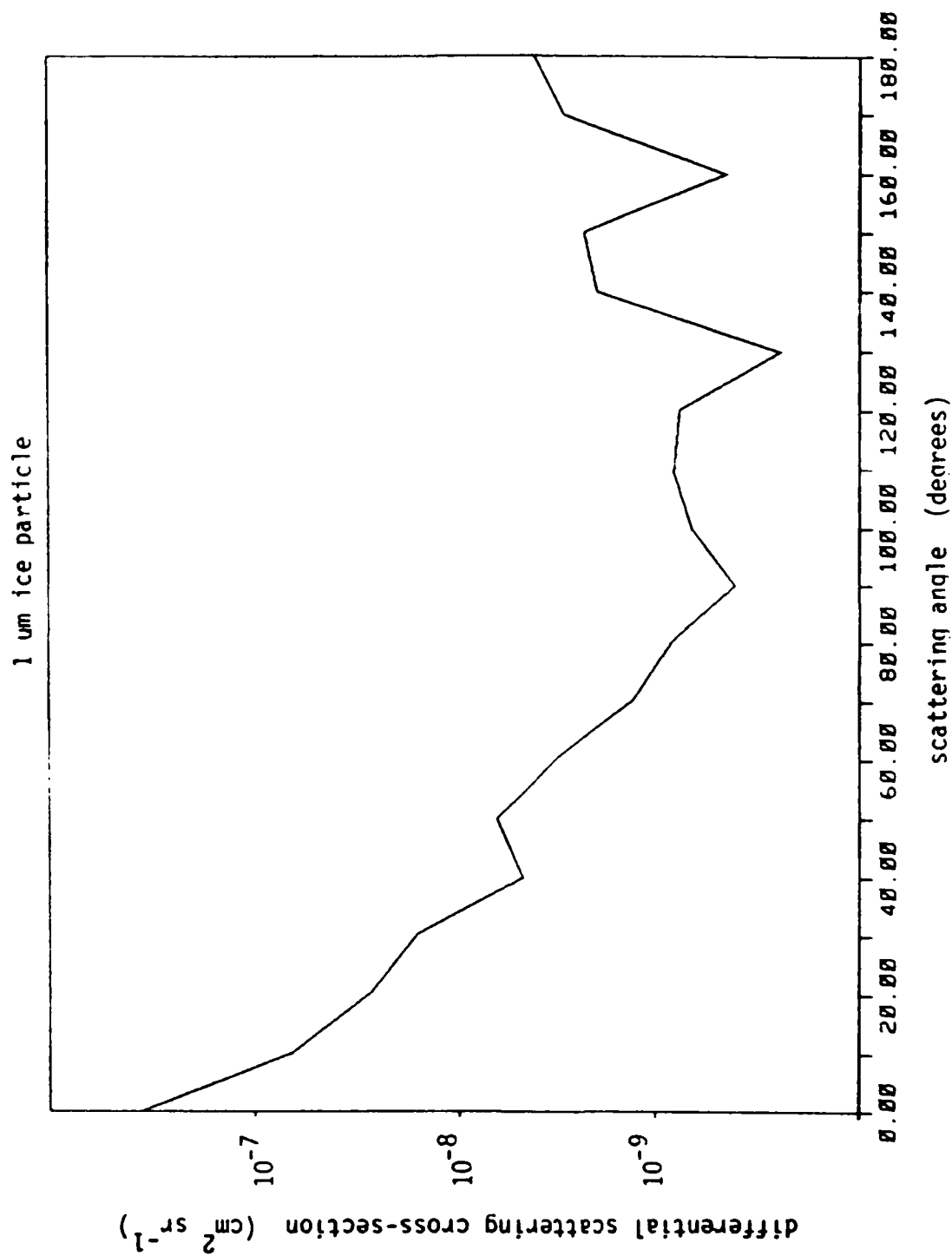


Figure 14a. Differential scattering cross-section for a one μm ice particle as a function of scattering angle. $\theta = 0$ is forward scattering.

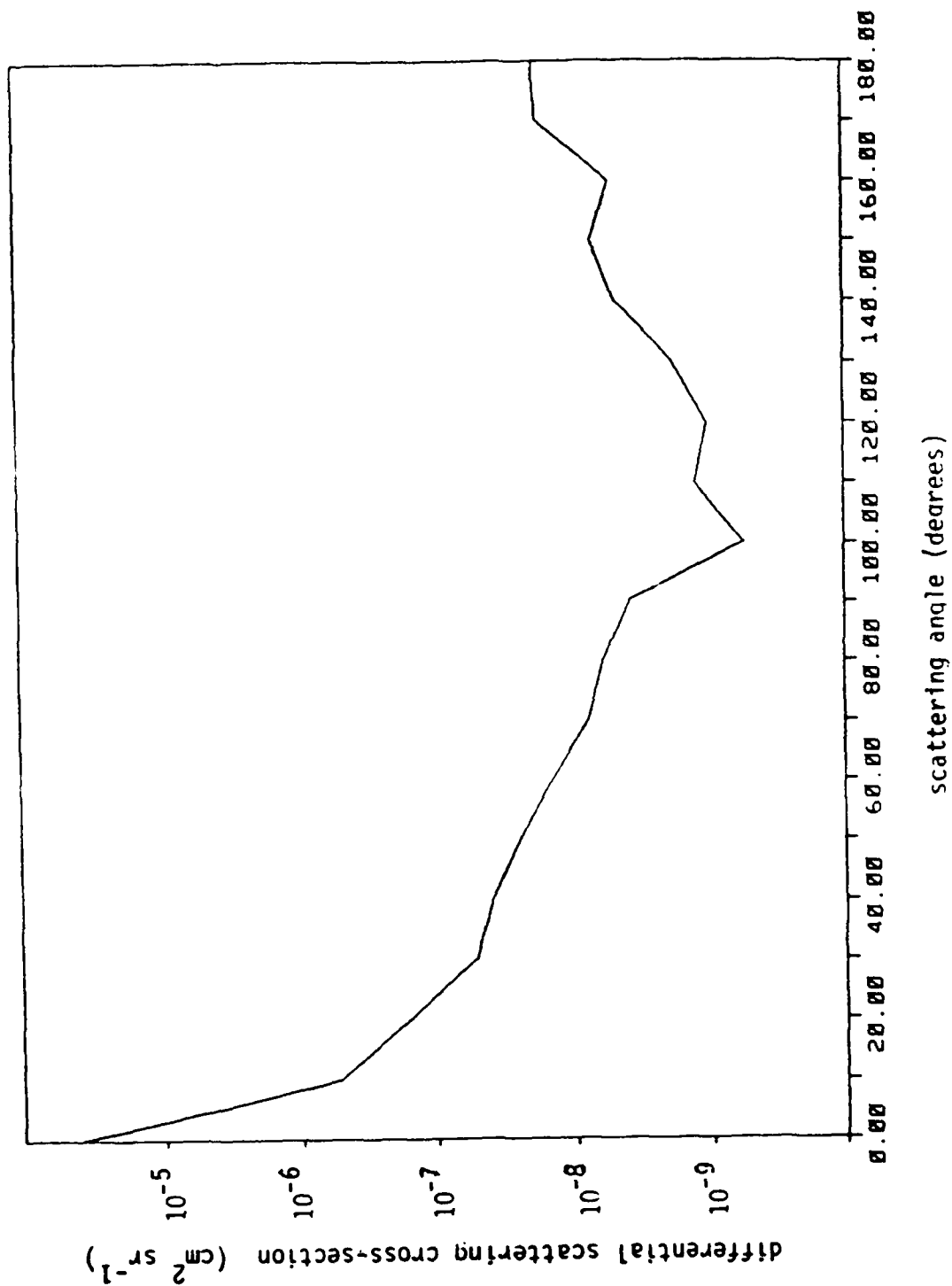
3 μm ice particle

Figure 14b. Differential scattering cross-section for a 3 μm ice particle as a function of scattering angle. 0 = 0 is forward scattering.

3.6 Calculations of Expected Signal Levels

3.6.1 Derivation of Signal/Noise Expression

The irradiance at the detector due to the scattering from a single particle at a given scattering angle is given by

$$H = f \cdot \frac{d\sigma}{d\Omega} \cdot \frac{1}{r^2}$$

where f is the incident flux expressed in photons $\text{cm}^{-2} \text{sec}^{-1}$, r is the distance from the scattering particle to the detector expressed in cm and $d\sigma/d\Omega$ is the partial differential scattering cross-section expressed in $\text{cm}^2 \text{sr}^{-1} \text{particle}^{-1}$.

The irradiance at the detector for an equivalent diffuse source is given by

$$H = \frac{10^6 \cdot R \cdot \Omega_s}{4 \pi}$$

where Ω_s is the solid angle of the detector and R is the apparent surface brightness in Rayleighs. Equating these two expressions, we find that the equivalent brightness in Rayleighs produced by a single particle is

$$R = \frac{4\pi}{10^6} \cdot \frac{d\sigma}{d\Omega} \cdot f \cdot \frac{1}{\Omega_s r^2}$$

3.6.2 Particle Velocity Effect on Signal Level

Because the number of particles detected during each measurement is expected to be small, the effect of the particle velocity must be considered. Given a constant energy per pulse from the xenon lamp, the maximum signal will be obtained when the pulse width is short compared to the time required for the particle to traverse one pixel in the object plane. Conversely, this pulse width precludes any determination of the particle velocity.

If the pulse width is short in comparison to the pixel traversal time, then the signal per pixel resulting from that single particle is

$$S = f \cdot \frac{d\sigma}{d\Omega} \cdot \frac{A}{r^2} \cdot \eta \cdot T \cdot t_{\text{pulse}}$$

where f is the peak power of the lamp pulse expressed in photons $\text{cm}^{-2} \text{sec}^{-1}$, $d\sigma/d\Omega$ is the partial differential scattering cross-section expressed in $\text{cm}^2 \text{sr}^{-1} \text{particle}^{-1}$, r is the distance from the particle to the collection optics, A is the area of the collection optics, T is the filter transmission (50%) and t_{pulse} is the lamp pulse width. If the pulse width is long in comparison to the pixel traversal time then the particle will cross several pixels per lamp pulse. The signal is then given by

$$S = f \cdot \frac{d\sigma}{d\Omega} \cdot \frac{A}{r^2} \cdot \eta \cdot T \cdot t_{\text{pix}}$$

The pixel traversal time, t_{pix} , is given by

$$t_{\text{pix}} = \frac{x_{\text{pix}}}{v_{\text{hor}}}$$

where x_{pix} is the pixel size in the object plane and v_{hor} is the particle velocity component parallel to the object plane. Typical particle velocities range from 10 to 2000 cm sec^{-1} .

The number of dark counts per second per pixel, N , is given as 0.01 sec^{-1} . The number of noise counts resulting from an integration for a time t is then given by

$$N(t) = (N \cdot t)^{1/2} = 0.1 t^{1/2}$$

The noise due to the celestial background after an integration for a time t is given by

$$N(t) = (B_c \cdot A \cdot \Omega \cdot \Delta\lambda \cdot \frac{\lambda}{hc} \cdot \eta \cdot T \cdot t)^{1/2}$$

where B_c is the celestial spectral radiance of $6 \times 10^{-11} \text{ watts m}^{-2} \text{deg}^{-2} \mu\text{m}^{-1}$ at 5000 Å when looking perpendicular to the galactic plane⁽¹³⁾. Evaluation of this expression yields

$$N_{\text{Celest}} = 4.4 \cdot t_{\text{pulse}}^{1/2} \text{ pixel}^{-1} \text{ pulse}^{-1} \text{ (WFOV Detector)}$$

$$N_{\text{celest}} = 0.9 \cdot t_{\text{pulse}}^{1/2} \text{ pixel}^{-1} \text{ pulse}^{-1} \text{ (NFOV Detector)}$$

As an example, Figures 15a-b show the velocity dependence of the signal level for 3 μm and 1 μm ice particles for the two detectors under differing focusing conditions where a 10 msec pulse width and a 10 msec integration time are used. The 450 - 550 nm band of the xenon lamp is used as the incident beam (2×10^{19} photons sec^{-1}). The detector and incident beam are in the perpendicular geometry. Table VIII lists the parameters used in the examples.

With a 10 msec pulse width, particles having the slowest measured velocities (10 cm sec^{-1}) will traverse several pixels; however, particles having velocities of more than a few meters per second will cross the entire array in that time.

3.6.3 Estimation of Particle Detection Frequency

As discussed in section 3.4, several measurements of spaceborne particulate contamination have been made. The conditions under which these measurements were made vary greatly as do the results (see Table VI).

In order to predict a particle detection rate for the MSX, a model must be developed to describe the shuttle particle measurements in terms of an "outgassing" rate. The preliminary model described in this section uses a Monte-Carlo technique to interpret the shuttle measurements and then applies the results to the MSX.

The open payload bay doors of the shuttle are approximated by a flat sheet $L = 2200 \text{ cm}$ long and $W = 460 \text{ cm}$ wide (see Figure 16). The field of view of the camera is described by a cone of half-angle Θ_0 , placed in the center of the flat sheet and described by

$$\cos(\Theta_0) = \frac{z}{r} = \frac{z}{(x^2 + y^2 + z^2)^{1/2}}$$

A random point ($x_g, y_g, z_g = 0$) is chosen for the initial location of a particle on the flat sheet. The particle's trajectory is described by direction cosines, chosen via a Monte Carlo technique

$$\frac{x - x_g}{\cos \alpha} = \frac{y - y_g}{\cos \beta} = \frac{z - z_g}{\cos \gamma}$$

3 μm ice particle
 10 msec pulse
 10 msec integration time

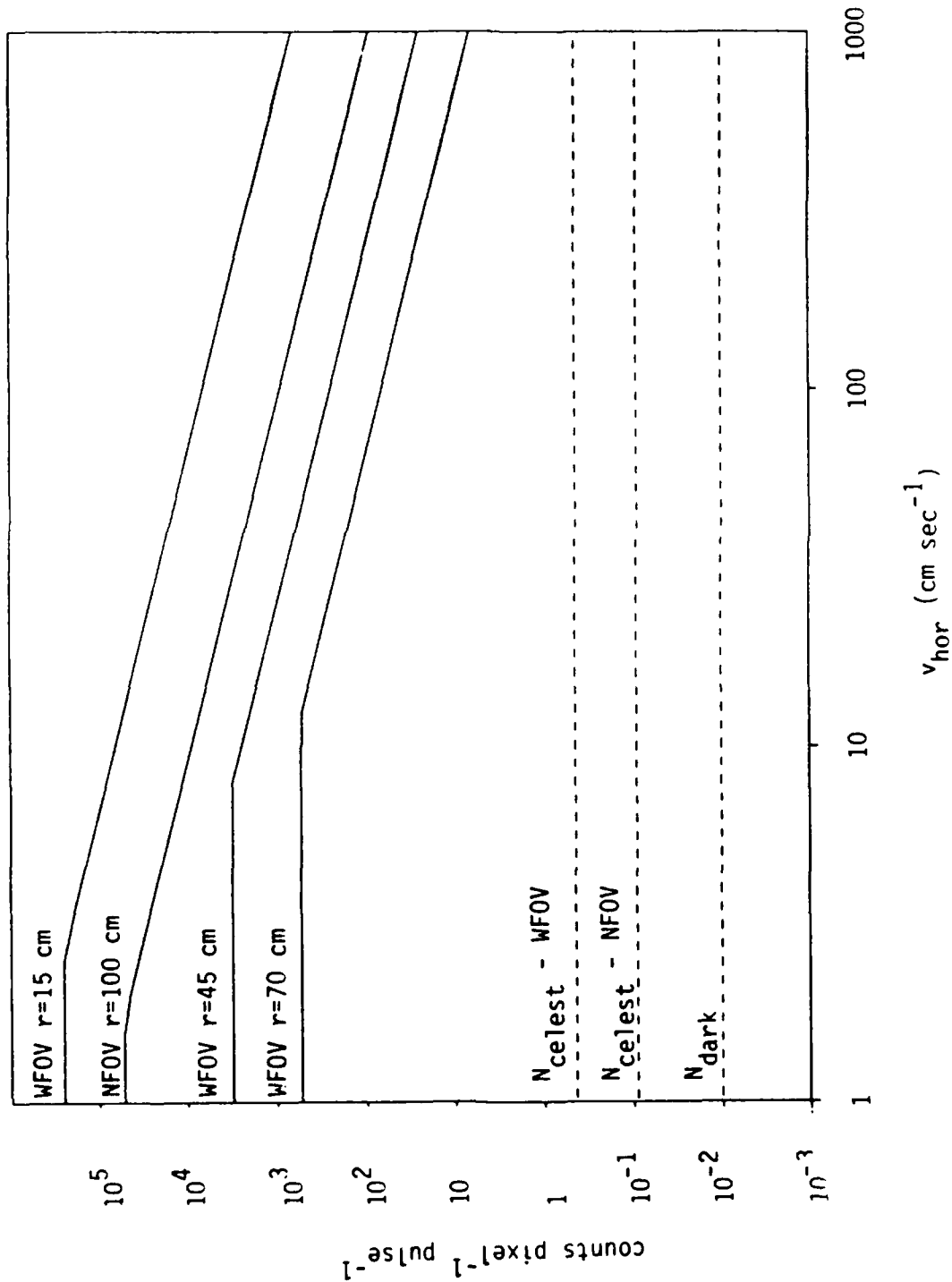


Figure 15a. Detected signal from a single 3 μm particle in a single pixel as a function of particle velocity for the NFOV imager focused at 100 cm and for the WFOV imager focused at 15 cm and 45 cm. The incident beam fills the field of view for all examples.

1 μm ice particle
 10 msec pulse
 10 msec integration time

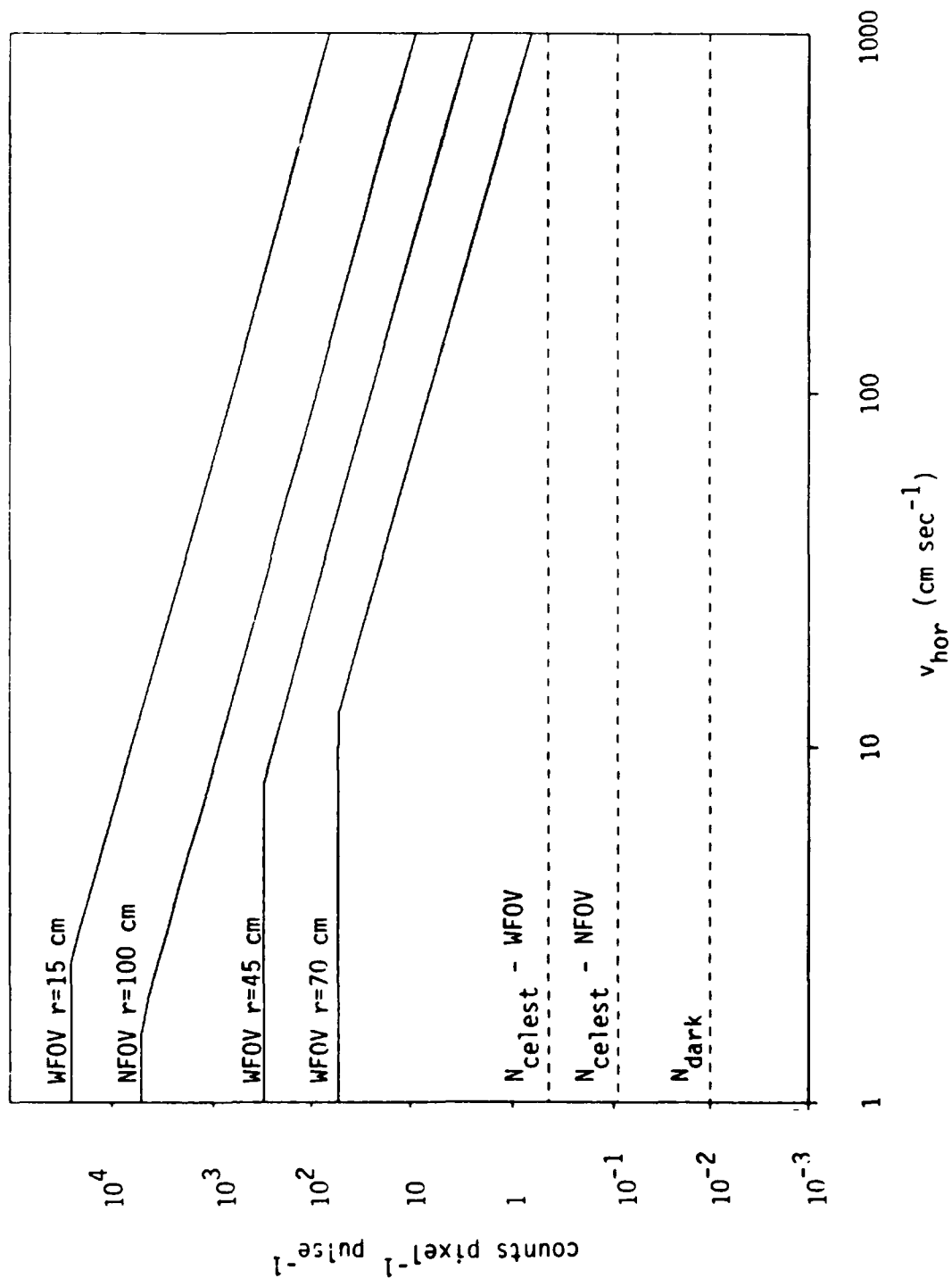


Figure 15b. Detected signal from a single 1 μm particle in a single pixel as a function of particle velocity for the NFOV imager focused at 100 cm and for the WFOV imager focused at 15 cm and 45 cm. The incident beam fills the field of view for all examples.

Table VIII

Examples Used for the Signal-to-Noise Calculation Shown in
 Figures 15a-b. Perpendicular Geometry is Assumed and the Beam Fills the
 Field of View. x_{pix} is the Spatial Extent of the Pixel in the Object Plane

<u>Perpendicular Geometry</u>				
<u>Detector</u>	<u>Focus(cm)</u>	<u>x_{pix} (cm)</u>	<u>beam diameter (cm)</u>	<u>$f(\text{phot cm}^{-2} \text{s}^{-1})$</u>
NFOV	100	1.8×10^{-2}	5	1×10^{18}
WFOV	15	2.6×10^{-2}	8	4×10^{17}
WFOV	45	7.9×10^{-2}	14	1.3×10^{17}
WFOV	70	1.2×10^{-2}	22	5.3×10^{16}

- Incident Beam Fills Detector FOV

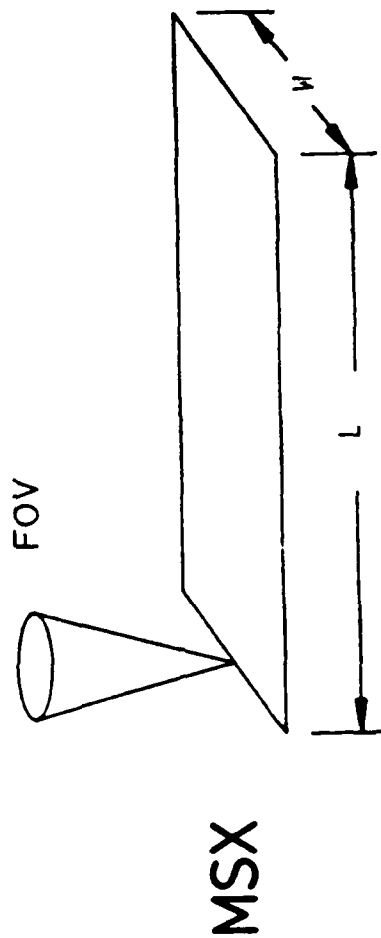
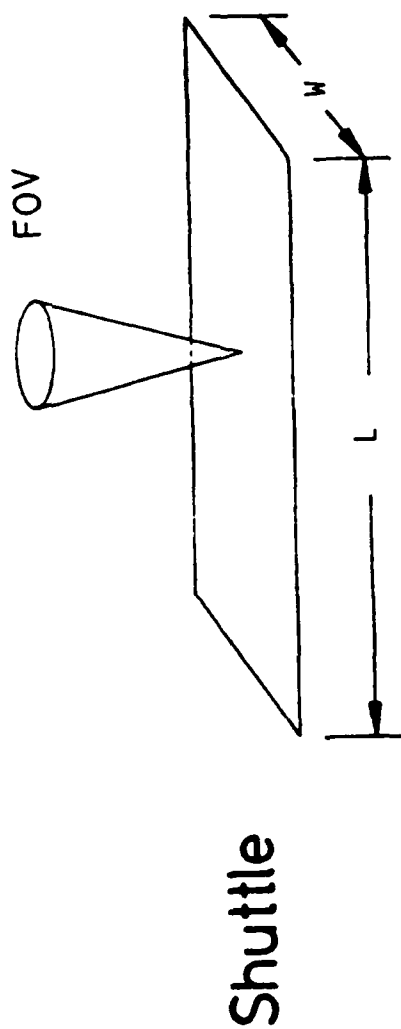


Figure 16. The open shuttle payload bay doors are modeled as a flat sheet $L = 2200$ cm and $W = 460$ cm wide. The detector field of view is modeled as a cone placed in the center of the sheet. The end of the MSX payload is modeled as a flat sheet $L = 200$ cm long by $W = 200$ cm wide. The detector field of view is modeled as a cone placed at the center of one edge of the sheet.

The direction cosines are chosen such that the particle trajectories will follow an isotropic distribution. We also have evaluated a Lambertian distribution which produced no significant differences in the results. The intersection of the trajectory with the field of view is obtained by combining the previous equations.

$$Z^2 \left[\frac{1}{\cos^2 \theta_0} - \left(\frac{\cos \alpha}{\cos \gamma} \right)^2 - \left(\frac{\cos \beta}{\cos \gamma} \right)^2 - 1 \right] + Z \left[2 x_g \frac{\cos \alpha}{\cos \gamma} + 2 y_g \frac{\cos \beta}{\cos \gamma} \right] + [-x_g^2 - y_g^2] = 0$$

The real solutions of this quadratic equation give the ranges at which the particle enters and exits the field of view. Many particles are started on the model surface and a histogram of the number entering the field of view as a function of range is generated.

The outgassing rate, or surface flux, is given by

$$F = \frac{N}{L \cdot W \cdot \Delta t}$$

where F is the surface flux expressed in particles $\text{cm}^{-2} \text{sec}^{-1}$, N is the number of particles started on the model surface, and Δt is some arbitrary length of time. The particle detection rate per solid angle, R_Ω , expressed in particles $\text{sec}^{-1} \text{sr}^{-1}$ is given by

$$R_\Omega = \frac{n_{fov}}{\Omega \cdot \Delta t}$$

where n_{fov} is the number entering the field of view at the required range and Ω is the solid angle of the detector. Rearrangement of the previous expressions yields the angular particle detection rate in terms of the surface flux.

$$R_\Omega = \frac{F \cdot L \cdot W \cdot n_{fov}}{N \cdot \Omega}$$

Thus our Monte Carlo simulation relates the measured quantity, R_{Ω} , to the quantity we would like to know, F .

In order to account for the different particle size detection limits of the various measurements, the above expression should be multiplied by a particle size distribution, $P(r)$. As discussed in section 3.4, early measurements indicated that the particle size distribution follows an $r^{-1.5}$ dependence. The number of particles detected, n_{det} , given a minimum detectable particle size, r_{min} , and a total number of particles entering the field of view, n_{fov} , is given by

$$n_{det} = n_{fov} \frac{\int_{r_{min}}^{\infty} r^{-1.5} dr}{\int_{r_p}^{\infty} r^{-1.5} dr}$$

$$n_{det} = n_{fov} \cdot \left(\frac{5}{r_{min}} \right)^{1/2}$$

where r_p is the particle size detection limit ($5 \mu m$) for the measurement from which this power law is derived.

When the minimum detectable particle size is taken into account, the expression for the flux becomes

$$F = \frac{R_{\Omega} \cdot \Omega}{L \cdot W} \left(\frac{N}{n_{fov}} \right) \left(\frac{r_{min}}{5} \right)^{1/2}$$

where R_{Ω} , Ω , L , W and r_{min} are taken from the experiment and N/n_{fov} is taken from the simulation.

This model provides a prescription for the interpretation of the particle detection rates as measured on the shuttle in terms of a universal quantity, the surface flux. The surface fluxes derived from the various shuttle measurements are summarized in Table IX. The fluxes derived from the infrared telescope (IRT-ST551F) measurements, from the Particle Analysis Cameras for shuttle (PACS - STS61C) and from the Induced Environment Contamination Monitor (IECM-STS2, 3, 4, 9) measurements are in fair agreement.

Table IX
Surface Fluxes and MSX Particle Detection Rates Derived
from Previous Shuttle Measurements Through the Monte Carlo Modeling

<u>Calculated Surface Fluxes</u>				Surface Flux*
<u>Mission</u>	<u>$R_n (s^{-1} \text{ sr}^{-1})$</u>	<u>Range (m)</u>	<u>$r_{min} (\mu m)$</u>	<u>$(cm^{-2} \text{ sec}^{-1})$</u>
IRT	390	20	70	8.6×10^{-5}
PACS	12	25	30	2.8×10^{-5}
IECM	0.39	50	25	4.3×10^{-6}

* Particle 5 Micron and Larger

Calculated MSX Detection Rates

10 msec Pulse, 20 Hz Repetition Rate, 180 sec Measurement
20 cm Diameter Beam
Perpendicular Geometry
WFOV $r = 150 \text{ cm}$

<u>$R(s^{-1})$</u>	<u>Average Detection Rate</u>	<u>Peak Detection Rate</u>
1.3×10^{-1}	2.9 Measurement ⁻¹	45 Measurement ⁻¹
4.2×10^{-2}	0.95 Measurement ⁻¹	14 Measurement ⁻¹
6.5×10^{-3}	0.15 Measurement ⁻¹	2 Measurement ⁻¹

10 msec Pulse, 20 Hz Repetition Rate, 180 sec Measurement
6 cm Diameter Beam
Perpendicular Geometry
NFOV $r = 200 \text{ cm}$

<u>$R(s^{-1})$</u>	<u>Average Detection Rate</u>	<u>Peak Detection Rate</u>
9.8×10^{-3}	0.35 Measurement ⁻¹	5.3 Measurement ⁻¹
3.2×10^{-3}	0.12 Measurement ⁻¹	1.7 Measurement ⁻¹
4.9×10^{-4}	0.018 Measurement ⁻¹	0.27 Measurement ⁻¹

These surface fluxes are used to predict particle detection rates for the MSX by using a similar model. The cone which represents the detector field of view in the model is placed at the edge of a flat sheet $L = 200$ cm long and $W = 200$ cm wide (see Figure 16). The algorithm used for finding n_{fov} as a function of range from the shuttle experiments is also used for the MSX. The calculated MSX particle detection rates for: (1) the WFOV detector and a 20 cm diameter incident beam in the perpendicular geometry at a range of 150 cm, and (2) the NFOV detector and a 6 cm diameter incident beam in the perpendicular geometry at a range of 200 cm are also summarized in Table IX.

The measurement sequence will have a duration of 180 seconds and will consist of 10 msec pulses at 20 Hz repetition rate from a 500 W xenon lamp. The calculated particle detection rates for the WFOV detector correspond to average particle detection rates of 0.2 - 3 per measurement. Since the peak detection rates are fifteen-fold higher than the average rates, we can expect detection rates as high as 2-45 per measurement sequence.

3.7 Preliminary Flight Specifications

A preliminary estimate of the engineering specifications for the particulate contamination experiment is given in Table X. The xenon lamp and power supply will occupy a box approximately 6 x 6 x 16 inches and weigh approximately 15 pounds. The average power requirement will be 100 W. The data requirements are also given in Table X. Eight bit resolution is required on various monitoring channels. Specifically, the power supply electrical properties, the power supply temperature and the lamp flux must be monitored.

3.8 Topics Requiring Further Study

Several items require further study before implementation of the particulate contamination experiment. The optical geometry and focusing effects must be analyzed in detail to develop a strategy for final optimization. The xenon lamp and power supply prototype must be fabricated and tested to determine the actual flux, input power requirements, cooling requirements and the expected lifetime of the system. Finally, the actual experimental payload must be designed and reviewed.

Table X
Preliminary Engineering Specifications for the Xenon Unit

Weight	15 lbs.	
Size	6 in. x 6 in. x 16 in.	
Power (Avg)	100 W	
Data Requirements (Power Supply)	Samples/Sec	Resolution (Bits)
28 VDC Voltage Monitor	<1	8
Source Voltage Monitor	4	8
Source Current Monitor	4	8
Power Supply Temperature Monitor	<1	8
Source UV Flux Monitor	20	8
Controls		
Source On/Off		
Pulse Synchronization		
Detector On/Off		
Detector Test		

4. EXPERIMENTAL OPERATION

A proposed operational experiment for the detection of particulate contamination and water vapor contamination is as follows. One measurement sequence consists of 100 seconds of water vapor data followed by 180 seconds of particulate matter data. Initial orbital checkout of the experiment consists of four sequences per orbit on alternate orbits. Prior to the opening of the door on the cryogenically cooled infrared sensor the following sequence would occur. Eight sequences per orbit on alternate orbits would be taken until such a time as the contaminant concentration be deemed low enough to open the door. After the infrared sensor is exposed, eight sequences on one orbit per day would be taken as a monitor of the contaminant concentration.

5. SUMMARY AND CONCLUSIONS

Experimental techniques for measuring water vapor and particulate contamination in a spacecraft environment are outlined. Both experiments are feasible with existing or modified commercially available technology.

For the water vapor experiment, the noise due to the celestial background is the dominant noise term. With the celestial background noise, the Krypton Radiometer has a detection limit ($S/N = 1$) of 6×10^6 H_2O molecules cm^{-3} for a 100 sec integration. If the celestial background is blocked, the noise due to the PMT dark current is the dominant noise contribution and the detection limit becomes 9×10^4 H_2O molecules cm^{-3} . These detection limits are several orders of magnitude lower than the measured shuttle H_2O concentrations. The Krypton Radiometer provides a small, inexpensive integral unit which will provide a sensitive and efficient measure of the H_2O concentration.

The APL Imaging spectrometer will provide a spectral signature for the OH ($A \rightarrow X$) emission and will reveal if any other species are emitting. There is a thirty fold advantage in sensitivity for using the Imaging Spectrometer in the axial configuration rather than in the perpendicular configuration. The effect of using optics focused at infinity to view near field objects is relatively small - out-of-focus sensitivity is 30% of the in focus sensitivity. The Imaging Spectrometer is less sensitive than the Krypton Radiometer; however, the spectral resolution is highly desirable.

The particulate contamination experiment is expected to detect as many as 45 particles per measurement sequence during peak viewing times. The noise due to the celestial background is small. In the perpendicular geometry good signal-to-noise is obtained for particles as small as $0.5 \mu m$ with velocities as fast as several meters per second.

Further work is required to develop a strategy for optimizing the effective sensitive volume for particle detection. Tradeoffs between the NFOV and WFOV detectors must be examined. The depth of focus and the exact beam geometry must be considered. Further modeling will be required to determine the effects of out of focus particles and to determine the tracking of the particles as they pass through the field of view and go in and out of focus.

REFERENCES

1. JHU/APL Document SDO 9027, Midcourse Space Experiment (MSX) Conceptual Design Review, February 1989.
2. L.C. Lee, OH ($A^2 \Sigma^+ \rightarrow X^2 \Pi$) Yield from H_2O Photodissociation in 1050 - 1370 Å, J. Chem. Phys. 72 4334 (1980).
3. I.P. Vinogradov, and F.I. Vilesov, Luminescence of the OH ($A^2 \Sigma^+$) Radical During Photolysis of Water Vapor by Vacuum UV Radioation, Opt. Spek. 44 1119 (1978).
4. H. Okabe, Photodissociation of Nitric Acid and Water in the Vacuum Ultraviolet: Vibrational and Rotational Distributions of OH ($A^2 \Sigma^+$), J. Chem. Phys. 72 6642 (1980).
5. G. Herzberg, Molecular Spectra & Molecular Structure, II, (Van NostRand Reinhold, new York, 1966).
6. G. Herzberg, Molecular Spectra & Molecular Structure III, (Van NostRand Reinhold, New York, 1966).
7. R.L. Kelly, Atomic Emission Lines in the Near Ultraviolet; Hydrogen Through Krypton, NASA Technical Memorandum 80268.
8. B.D. Green, G.E. Caledonia & T.D. Wilkerson, The Shuttle Environment: Gases, Particulates, and Glow, J. Spacecraft, 22 500 (1985).
9. B.D. Green, G.K. Yates, M. Ahmajian, H. Miranda, The Particulate Environment Around the Shuttle as Determined by the PACS Experiment, SPIE 777, Optical System Contamination, Effects, Measurement & Control 2 (1987).
10. K.S. Clifton & J.K. Owens, Optical Contamination Measurements and Early Shuttle Missions, Applied Optics, 27 603 (1988).
11. D.G. Koch et al., Infrared Observations of Contaminants from Shuttle Flight 51-F, Adv. Space Res. 7 211 (1987).
12. E. Wolf & U. VonZahn, The Shuttle Environment: Effects of Thruster Firings on Gas Sensity and Composition in the Payload Bay, J. Geophys. Res. 91 3270 (1986).
13. C.W. Allen, Astrophysical Quantities (The Athlone Press, London, 1976).
14. H.C. van de Hulst, Light Scattering by Small Particles, (Dover, New York, 1981).
15. Oriel Catalog, Vol. II, Oriel Corp., Stratford, CT.